

Structure of the μ -opioid receptor–G_i protein complex

Antoine Koehl^{1,12}, Hongli Hu^{1,2,12}, Shoji Maeda^{2,12}, Yan Zhang^{1,2}, Qianhui Qu^{1,2}, Joseph M. Paggi^{1,2,3,4}, Naomi R. Latorraca^{1,2,3,4,5}, Daniel Hilger², Roger Dawson⁶, Hugues Matile⁶, Gebhard F. X. Schertler^{7,8}, Sébastien Granier⁹, William I. Weis^{1,2}, Ron O. Dror^{1,2,3,4,5}, Aashish Manglik^{10,11*}, Georgios Skiniotis^{1,2*} & Brian K. Kobilka^{2*}

The μ -opioid receptor (μ OR) is a G-protein-coupled receptor (GPCR) and the target of most clinically and recreationally used opioids. The induced positive effects of analgesia and euphoria are mediated by μ OR signalling through the adenylyl cyclase-inhibiting heterotrimeric G protein G_i. Here we present the 3.5 Å resolution cryo-electron microscopy structure of the μ OR bound to the agonist peptide DAMGO and nucleotide-free G_i. DAMGO occupies the morphinan ligand pocket, with its N terminus interacting with conserved receptor residues and its C terminus engaging regions important for opioid-ligand selectivity. Comparison of the μ OR–G_i complex to previously determined structures of other GPCRs bound to the stimulatory G protein G_s reveals differences in the position of transmembrane receptor helix 6 and in the interactions between the G protein α -subunit and the receptor core. Together, these results shed light on the structural features that contribute to the G_i protein-coupling specificity of the μ OR.

The μ OR is the primary target of morphine and many clinical opioid analgesics¹. Binding of opioids to the μ OR leads to clinically desired analgesic and antitussive actions, but also important negative side effects, including addiction and potentially lethal respiratory suppression. Opioids have become the most prescribed class of medication in the United States², which has led to a national epidemic of addiction and an unprecedented level of drug overdose deaths.

Like other GPCRs, the μ OR achieves many of its physiological actions by stimulating signalling via a heterotrimeric G protein. While other GPCRs have been shown to signal through more than one G-protein subtype, the μ OR signals almost exclusively through the adenylyl cyclase-inhibitory family of G proteins (G_{i/o})³. The analgesic activity of opioids is driven by G-protein activation⁴, but activated μ OR can also interact with β -arrestins, recruitment of which has been associated with the respiratory depression induced by many opioids^{5,6}. Recently developed molecules that favor G_i signalling over arrestin recruitment display analgesic efficacy with reduced side effects, suggesting that different signalling pathways can be selectively targeted to yield unique physiological outcomes^{7,8}. Although a framework for GPCR interactions with the stimulatory G protein G_s has recently been enabled by X-ray crystallography⁹ and cryo-electron microscopy (cryo-EM)^{10,11} studies, the structural basis of GPCR signalling through other G-protein subtypes remains undefined. To better understand the mechanism of selective activation of G_i by the μ OR, we sought to determine the structure of the μ OR–G_i complex.

3.5 Å cryo-EM map of a μ OR–G_i complex

DAMGO (H-Tyr-D-Ala-Gly-N(Me)Phe-Gly-OH) is a μ OR-selective synthetic analogue of the natural peptide agonist enkephalin. DAMGO-bound μ OR was incubated with G_{i1} heterotrimer, and the complex was treated with the nucleotide hydrolase apyrase to remove GDP.

The resulting nucleotide-free complex was further stabilized by a single-chain variable fragment (scFv16) that binds to heterotrimeric G_i (Extended Data Fig. 1) and prevents GTP γ S-mediated dissociation of nucleotide-free complexes. We applied single-particle cryo-EM to initially obtain a three-dimensional map of the μ OR–DAMGO–G_i–scFv16 complex at an indicated nominal resolution of 3.6 Å (Extended Data Figs. 2, 3, Extended Data Table 1). Notably, scFv16 binds a composite interface comprised of the α N helix of G α _i and the β -propeller of G β , a site that is more than 20 Å distal to the μ OR–G α _i interface and does not perturb the interface between G α and G β subunits (Extended Data Fig. 1). Subtraction of the scFv16 signal from raw particle images led to an improved map with an indicated global resolution of 3.5 Å. This map displayed enhanced features, particularly in the transmembrane core of the receptor (Extended Data Figs. 2–4), which enabled the high-resolution visualization of the μ OR–G_i interface and ligand binding. Accordingly, we employed this improved 3.5 Å map to examine interactions between μ OR and DAMGO, and between μ OR and G_i (Fig. 1a, b).

Activation of μ OR by a peptide agonist

The active-state crystal structure of μ OR bound to the morphinan agonist BU72 and an active-state stabilizing nanobody (Nb39) has been determined at a resolution of 2.2 Å¹². Similar to other small molecule morphinans, BU72 is rigidified by a complex ring system; in contrast to flexible opioid peptides, such as DAMGO, that have multiple rotatable bonds. Our cryo-EM map includes well-defined features for most amino acids forming the orthosteric binding pocket (Extended Data Fig. 4a). Despite differences in agonist structure, the conformation of the active-state ligand-binding pocket and the orientation of the amino acids that interact with the agonist are highly similar between the μ OR bound to either BU72 or DAMGO (Fig. 1c),

¹Department of Structural Biology, Stanford University School of Medicine, Stanford, CA, USA. ²Department of Molecular and Cellular Physiology, Stanford University School of Medicine, Stanford, CA, USA. ³Department of Computer Science, Stanford University, Stanford, CA, USA. ⁴Institute for Computational and Mathematical Engineering, Stanford University, Stanford, CA, USA. ⁵Biophysics Program, Stanford University, Stanford, CA, USA. ⁶Roche Pharma Research and Early Development, Therapeutic Modalities, Roche Innovation Center Basel, F.Hoffmann-La Roche, Basel, Switzerland. ⁷Laboratory of Biomolecular Research, Paul Scherrer Institute, Villigen, Switzerland. ⁸Department of Biology, ETH Zürich, Zürich, Switzerland. ⁹Institut de Génomique Fonctionnelle, INSERM, Montpellier, France. ¹⁰Department of Pharmaceutical Chemistry, University of California San Francisco, San Francisco, CA, USA. ¹¹Department of Anesthesia and Perioperative Care, University of California San Francisco, San Francisco, CA, USA. ¹²These authors contributed equally: Antoine Koehl, Hongli Hu, Shoji Maeda. *e-mail: Aashish.Manglik@ucsf.edu; yiorgo@stanford.edu; kobilka@stanford.edu

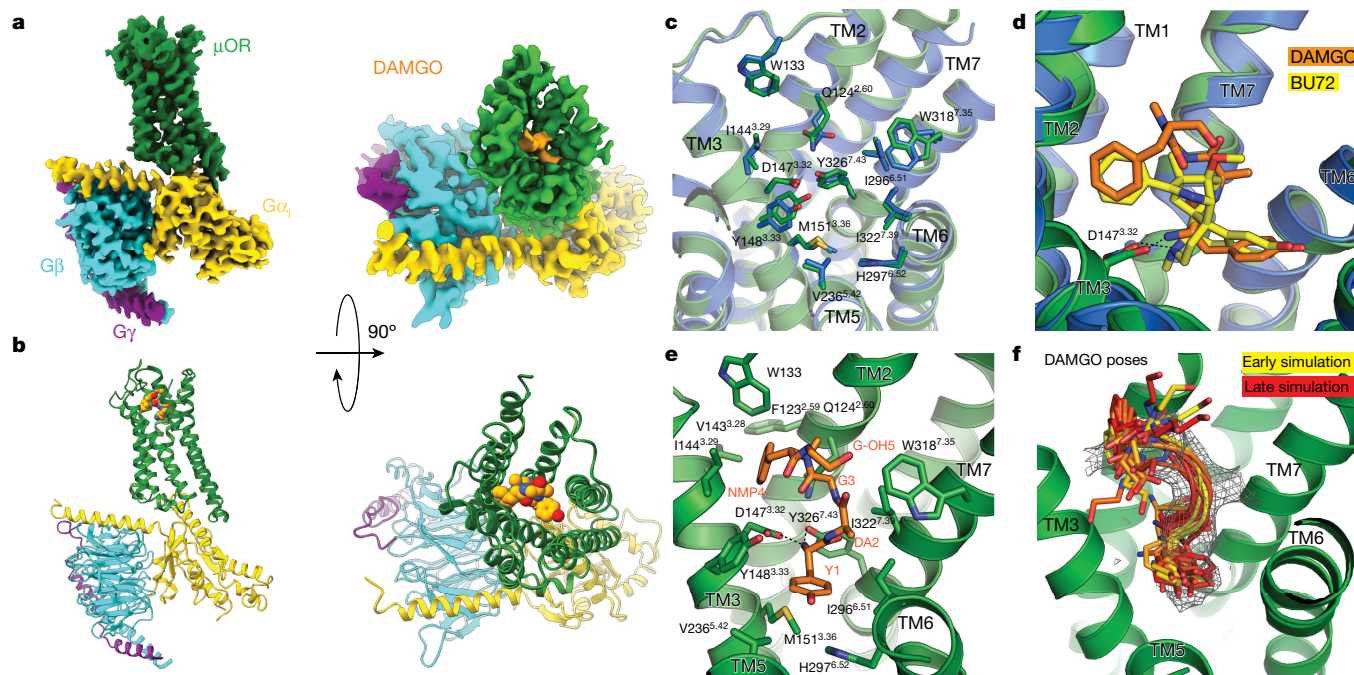


Fig. 1 | Cryo-EM structure of the μ OR- G_i complex. **a**, Orthogonal views of the cryo-EM density map of the μ OR- G_i heterotrimer complex coloured by subunit. Green, μ OR; orange, DAMGO; gold, $G\alpha_i$ Ras-like domain; cyan, $G\beta$; purple, $G\gamma$. **b**, Model of the μ OR- G_i complex in the same views and colour scheme as shown in **a**. **c**, Residues that line the μ OR orthosteric binding pocket are shown as sticks for the μ OR- G_i complex (green) and the μ OR-Nb39 complex (PDB code 5C1M; blue). The binding pocket residues of μ OR in complex with DAMGO and BU72 show nearly identical conformations, despite differences in ligand structure. **d**, Comparison

suggesting that the μ OR recognizes structurally distinct agonists in a stereotyped manner.

Although DAMGO is a flexible ligand, we observe density for the entire peptide bound to the receptor (Fig. 1a, Extended Data Figs. 3, 4). The N terminus of DAMGO occupies a similar position in the binding pocket as BU72. By contrast, the C terminus of DAMGO extends ~8 Å further towards the extracellular loops compared to BU72 (Fig. 1d, e). To identify stable atomic-level interactions between DAMGO and the binding pocket, we performed molecular dynamics simulations. In over 1 μ s of simulation, DAMGO remained close to its initially modelled pose, with the N-terminal portion largely remaining confined to the experimentally determined cryo-EM density (Fig. 1f, Extended Data Fig 5). The N terminus of DAMGO maintained a persistent salt bridge with D147^{3,32}, a feature previously observed in structures of morphinans bound to opioid receptors (Fig. 1e; superscripts indicate Ballesteros–Weinstein numbering for GPCRs¹³). The same amine group also frequently formed a hydrogen bond with Y326^{7,43}. More generally, the N-terminal Tyr of DAMGO overlaps the phenolic groups of other small-molecule opioids that have been characterized in complex with μ OR or other opioid receptors by X-ray crystallography^{14–17}.

Molecular dynamics simulations also revealed a water-mediated hydrogen bonding network that closely overlaps with the water network observed in the high-resolution crystal structure of μ OR¹² (Extended Data Fig. 6). In particular, the simulations revealed a stable, water-mediated interaction that is formed between the phenol of DAMGO and H297^{6,52}. Although the crystal structure of the μ OR bound to BU72 shows two water molecules bridging the DAMGO phenol and H297^{6,52}, simulations of μ OR bound to DAMGO and other phenolic ligands^{8,12} suggest that one of these water molecules rapidly dissociates, and that a single water is required for stable ligand binding. This interaction is a hallmark of opioid recognition that has been observed for morphinans in complex with the μ OR^{12,14} as well as other small

of BU72 (yellow carbons) in the orthosteric pocket of the μ OR-Nb39 complex (blue) with DAMGO (orange carbons) in the orthosteric pocket of the μ OR- G_i complex (green). **e**, view of DAMGO in the orthosteric binding pocket with critical residues shown. **f**, A frame from every 100 ns of a 1 μ s molecular dynamics simulation (yellow at $t = 0$, fading to red at $t = 1 \mu$ s) shows that the first four residues of DAMGO (bottom) are stable, whereas the C-terminal Gly-ol (top) is dynamic but frequently returns to the modelled pose.

molecule and peptide-mimetic agonists of the homologous δ - and κ -opioid receptors (δ OR and κ OR)^{15,16,18}.

DAMGO exhibits more than 500-fold selectivity for the μ OR over the δ OR and κ OR¹⁹. Structural studies have shown that interactions of ligands with the extracellular loops encode ligand subtype specificity among closely related opioid receptors¹⁵. Indeed, DAMGO selectivity for μ OR over δ OR has been shown to depend on residues in extracellular loop (ECL) 1, whereas selectivity over κ OR results from differences in ECL3²⁰. The map density for the C-terminal residues of DAMGO is slightly weaker than for the amino terminus, consistent with increased mobility of this region in simulations (Fig. 1f, Extended Data Fig 5). In our model, the N(Me)Phe side chain of DAMGO occupies a conserved hydrophobic pocket near ECL1 and the Gly-OH group folds back over the ligand (Fig. 1e). This model is consistent with the high affinity of μ OR binding to cyclized enkephalins, which bridge the +2 and +5 positions of the peptide²¹.

Structure of G_i -stabilized active μ OR

The overall structure of G_i -bound μ OR is similar to the active conformation of the BU72-bound μ OR stabilized by Nb39¹² (root mean square deviation of 1 Å) with a predominant outward displacement of transmembrane helix (TM) 6 from the heptahelical bundle relative to the inactive state (Fig. 2a, b). A number of highly conserved residues in the GPCR family have been shown to be important for receptor activation, including the D^{3,49}R^{3,50}Y^{3,51}, N^{7,49}P^{7,50}XXY^{7,53} and conserved core triad (I^{3,40}, P^{5,50}, F^{6,44}) motifs. The conformation of each of these regions in the μ OR- G_i complex is virtually identical to the active state observed in the complex with Nb39 (Fig. 2c). The structural similarity of μ OR between Nb39 and G_i -bound states indicate that these changes underlie ligand-mediated activation and are not specific to a particular intracellular binder. Indeed, Nb39 and G_i promote a similar increase in agonist affinity¹², supporting a common mechanism of allosteric communication between the intracellular G-protein-coupling domain and the ligand-binding pocket¹².

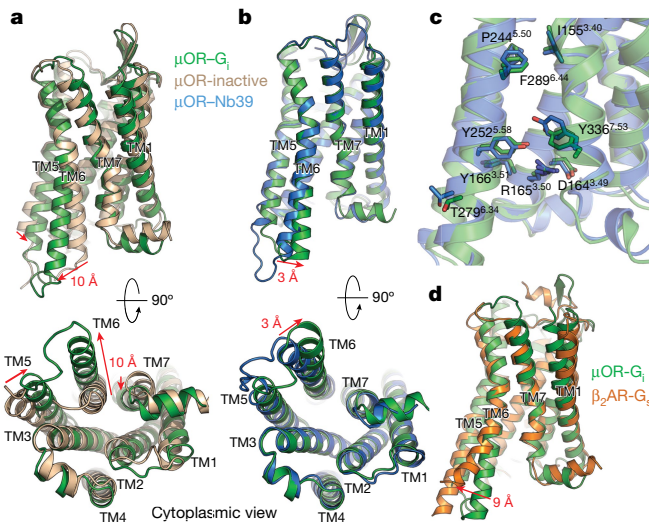


Fig. 2 | Structural changes in the μ OR stabilized by nucleotide-free G_i . **a**, Comparison of inactive μ OR (brown) and the G_i -stabilized active state of μ OR (green). **b**, Comparison of Nb39-stabilized and G_i -stabilized active states of the μ OR (blue and green, respectively). The structures are nearly identical except for a slight shift of TM6 towards TM7 in the G_i -bound state. **c**, Residues important for activation of the μ OR show nearly identical conformations despite the difference in ligands. **d**, Comparison of G_i -stabilized β_2 AR (orange) and G_i -stabilized μ OR (green). While most transmembrane helices align well between the two receptors, TM6 is kinked further outward by 9 Å in the β_2 AR; this distance is calculated between positions of C_α of residue 6.29 (Ballesteros–Weinstein numbering) in TM6.

Two differences between Nb39- and G_i -stabilized active states of μ OR are particularly notable. First, compared with the nanobody-stabilized active-state μ OR, TM6 in the μ OR– G_i complex is further displaced by 3 Å towards TM7 (Fig. 2b). Second, the conformation of intracellular loop (ICL) 3 is different between the two structures (Fig. 2b). It is likely that the specific ICL3 conformation of Nb39-stabilized μ OR reflects interactions that are unique to the nanobody rather than a general feature of receptor activation prior to G-protein coupling. A similar difference in ICL3 conformation was previously observed for the β_2 -adrenergic receptor (β_2 AR) between nanobody²² (Nb80) and G_s -coupled states. The comparison of the G-protein-bound states of both receptors shows that TM6 of β_2 AR is displaced outward by a further 9 Å in comparison to that of the μ OR (Fig. 2d).

Structural changes in G_i

The quality of the cryo-EM map enabled accurate modelling of G_i in its nucleotide-free state, providing insight into the structural changes

that underlie nucleotide release. The changes are similar to those seen in nucleotide-free G_s in complex with other GPCRs. The most striking difference between the GDP-bound²³ and nucleotide-free heterotrimer in complex with μ OR involves the separation of the α -helical domain (AHD) from the Ras-like domain in $G\alpha_i$ (Fig. 3a). Owing to its relative flexibility, we excluded the AHD density from the high-resolution map refinement. The dynamic character of the AHD has been observed previously in spectroscopic and structural studies of complexes between receptors and G_s ^{9–11} and G_i ^{24,25}. Displacement of the AHD disrupts several contacts with GDP and is necessary, but not sufficient, for nucleotide release, a process that involves breaking additional contacts with the Ras domain²⁴.

Coupling of G_i to the μ OR also involves a 6 Å translation as well as a 60° rotation of the α 5-helix of $G\alpha_i$ into the receptor core (Fig. 3b). This movement has been shown to be essential for nucleotide release by G_i ²⁴. In particular, the movement of α 5 leads to a change in the position of the β 6– α 5 loop containing the conserved TCAT motif that forms direct interactions with the guanine base of GDP. This displacement disrupts key contacts between the G protein and nucleotide. Furthermore, the observed translation and rotation of the α 5-helix requires the displacement of the fully conserved F336 away from the hydrophobic pocket formed by residues in the β 2 and β 3 strands and the α 1 helix²⁶ (Fig. 3b). Movement of the α 5-helix is also propagated to the phosphate-binding P loop connecting the β 1 strand and the α 1 helix by disruption of a hydrophobic network between the α 1 and α 5 helices (Fig. 3b–d). Correspondingly, upon transition of G_i to the nucleotide-free state, we observe a 4 Å shift of α 1 towards the α 5-helix in G_i whereby the hydrophobic contacts are replaced by polar interactions with the β 6– α 5 loop as it is released from its guanine-binding position (Fig. 3c, d). These changes are in contrast to those observed in structures of G_s -coupled complexes, in which α 1 not only becomes more unstructured, but also tends to lose interactions with the α 5-helix (Fig. 3e). Our structure is consistent with previous studies suggesting that engagement of a GPCR with the α 5-helix and α N– β 1 loop leads to concerted changes in the α 1 helix and P loop that destabilize contacts with the guanine nucleotide, leading to its release²⁷.

Structural insights into G_i -coupling specificity of the μ OR

Although the μ OR couples exclusively to $G_{i/o}$ ³, many GPCRs can couple to multiple G-protein subtypes. A well-studied example is the β_2 AR, which couples to both G_s and $G_{i/o}$. Previous sequence-level analyses have failed to identify a linear GPCR epitope that determines G-protein-coupling specificity, suggesting that specificity is likely to be determined by a more complex three-dimensional network of interactions. Globally, the structure of the μ OR– G_i complex is similar to that of the β_2 AR– G_s complex; this is likely to reflect a similarity in the conformation of nucleotide-free states of family A GPCR–G-protein complexes. The primary interaction sites in

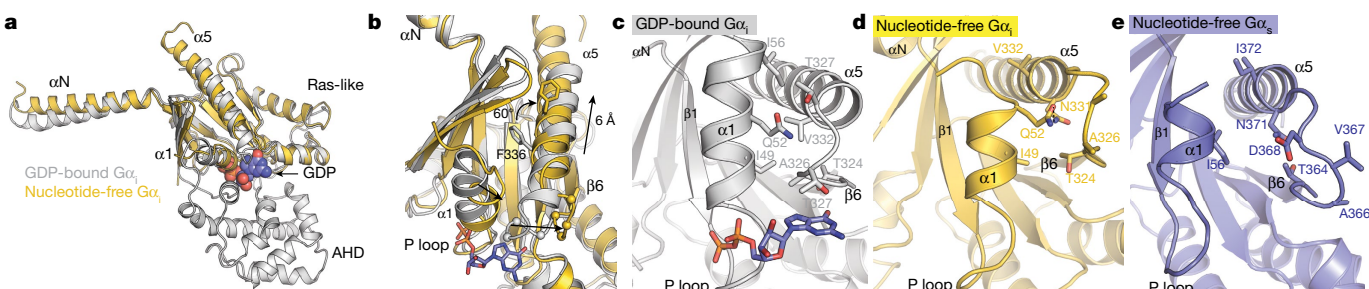


Fig. 3 | Changes in G_i upon coupling to the μ OR. **a, b**, Comparison of GDP-bound $G\alpha_i$ (PDB code 1GP2, grey) and nucleotide-free $G\alpha_i$ from the μ OR– G_i complex (gold). GDP is shown as blue spheres in **a** and sticks in **b** and **c**. The primary differences between these two structures are the opening and outward movement of the alpha helical domain (AHD), and an upward shift of the α 5-helix by 6 Å to engage the receptor core. The α -carbons of the TCAT motif are represented as spheres in **b**. The TCAT

motif coordinates the guanine base of GDP. The upward shift of the α 5-helix and repositioning of the TCAT motif leads to nucleotide release. **c, d, e**, The interface between the α 1 helix and the N-terminal end of the α 5-helix and TCAT motif for GDP-bound $G\alpha_i$ (**c**), nucleotide-free $G\alpha_i$ (**d**) and nucleotide-free G_s from the β_2 AR– G_s complex (**e**). The upward movement of the α 5-helix disrupts the interaction between the α 1- and α 5-helices, leading to changes in the P loop that coordinates the phosphates of GDP.

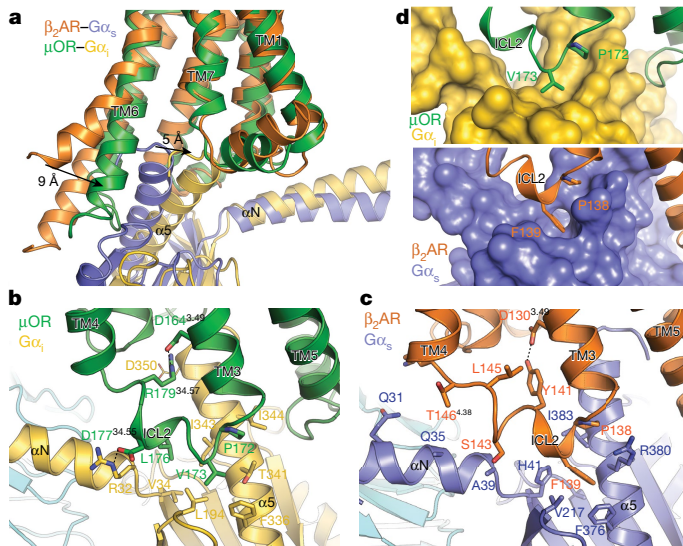


Fig. 4 | Comparison of the receptor-G-protein binding interfaces of the μ OR-G_i and β_2 AR-G_s complexes. **a**, Comparison of the conformation of the α 5-helix of G α and receptor TM6 in β_2 AR-G_s and μ OR-G_i complexes after alignment on the receptor. **b**, Interactions between ICL2 of the μ OR (green) and G α _i (gold). Asp 350 of G α _i is depicted with narrow lines to indicate uncertainty in its conformation due to poor cryo-EM density for its side chain. **c**, Interactions between ICL2 of the β_2 AR (orange) and G α _s (blue). **d**, Surface view of the hydrophobic pockets in G α _i (top panel) and G α _s (bottom panel) that interact with a non-polar amino acid in ICL2 of the μ OR and β_2 AR, respectively.

both complexes occur between ICL2, ICL3 and TM3, TM5 and TM6 on the receptor and the α N, α N- β 1 loop and α 5-helix on the G α subunit of the G protein (Fig. 4). The most striking differences between the β_2 AR-G_s and μ OR-G_i complexes are in the relative position of the α 5-helix of both G proteins and the corresponding shift in the position of TM6 in the receptor. The α 5-helix of G α _i is rotated $\sim 21^\circ$ relative to the α 5-helix of G α _s, leading to a 5 Å displacement of the extreme C terminus of the G α _i helix α 5 toward TM7 of the μ OR (Fig. 4a). This difference in α 5 positioning is associated with a smaller outward displacement of the μ OR TM6. The C-terminal residues of α 5 that interact with TM5 and TM6 of the receptor are bulkier in G_s than in G_i, with tyrosine and glutamate in place of cysteine and glycine at positions -4 and -3 from the C terminus, respectively. Accordingly, substitution of these two amino acids of G_s into G_i would lead to steric clashes with TM3 and the TM7-helix 8 loop (Extended Data Fig. 7). In the G_s-coupled family B calcitonin¹¹ and GLP-1¹⁰ receptors, G-protein coupling is associated with a large kink of TM6 at the conserved PXXG motif, which produces an even larger outward displacement of TM6 than that observed in the β_2 AR-G_s complex.

Surprisingly, the structure of μ OR-G_i shows substantial similarity to an active-state structure of the visual pigment rhodopsin (metarhodopsin II) in complex with a modified peptide derived from the 11 C-terminal residues of the α -subunit of the visual G protein transducin (G α _tCT2)²⁸ (Extended Data Fig. 8). Despite the absence of the rest of the heterotrimeric G protein in the metarhodopsin II-G α _tCT2 structure, the conformation of TM6 of metarhodopsin II is highly similar to that of the μ OR, and the location of the G α _tCT2 peptide is almost identical to that of the C terminus of G α in complex with μ OR. This finding is consistent with observations showing that substitution of the last five amino acids of the α 5-helix of G α is sufficient to change G-protein-coupling specificity²⁹.

In Extended Data Table 2, we list amino acids in the μ OR that interact with the cytoplasmic surface of G α . The ICL2 of μ OR primarily forms interactions with the α N and α 5 helices of G α _i, including a key ionic interaction between D177^{34,55} of μ OR (G Protein Coupled Receptor Data Base (GPCRDB) numbering³⁰) in ICL2 and R32 in the α N- β 1 loop of G α _i (Fig. 4b). Although D^{34,55} in ICL2 is conserved in all opioid receptors with available sequences (GPCRDB³¹), it is variable in most other G α -coupled receptors. Another notable interaction involves R179^{34,57} in ICL2 of μ OR, which simultaneously coordinates the highly conserved D164^{3,49} in the D^{3,49}R^{3,50}Y^{3,51} motif and potentially forms an additional interaction with D350 (-5 position) in the α 5-helix of G α _i (Fig. 4b). This arginine residue is essential for μ OR-induced G α signalling, as the polymorphic variant R179C abolishes signalling in vitro³² and leads to insensitivity to morphine in patients homozygous for the mutation³³. The potential role of this interaction network in G-protein coupling is supported by the preponderance of basic residues (arginine and lysine) at this position in most G α -coupled receptors, whereas G_s-coupled receptors contain alternative residues at the equivalent position (Extended Data Table 2).

A further group of contacts occurs between P172^{34,50} and V173^{34,51} of μ OR and a hydrophobic patch on G α _i comprised of residues F336, I343, I344 and T340 on the α 5-helix and L194 on the β 2- β 3 loop (Fig. 4b, d). In the GDP bound state, these α 5-helix residues are buried by the adjacent β 2 and β 3 loops. Coupling to a receptor involves an upward shift of the α 5-helix and exposes these residues to form a shallow hydrophobic pocket that interacts with μ OR V173^{34,51} in ICL2 (Fig. 4b, d). In the case of G_s, a deeper hydrophobic pocket in this region engages the bulky aromatic F139^{34,51} in ICL2 of the β_2 AR (Fig. 4c, d).

In the μ OR, ICL3 stabilizes the interface between receptor and G protein through two sets of interactions: one set involves multiple contacts with a hydrophobic patch on the α 5-helix of G α _i, while another engages the β 6 strand of G α _i through a network of charged residues (Fig. 5a, c). The hydrophobic interface formed by ICL3 is similar in both the μ OR and β_2 AR; in the β_2 AR, TM5 is helically extended to form a larger hydrophobic interaction around nonpolar residues in the α 5-helix of G α _s (Fig. 5b). The shorter ICL3 of the μ OR does not form a similar helical extension, but it nevertheless fulfills the same role. Residues V262^{5,68}, M264 and L265 fold back to form a hydrophobic patch that interacts with hydrophobic residues on the α 5-helix of G α _i (Fig. 5a).

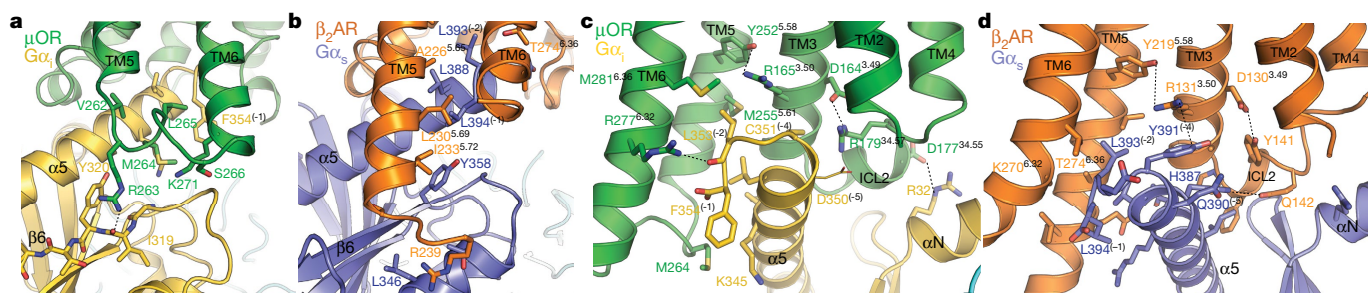


Fig. 5 | Comparison of the receptor-G-protein binding interfaces of the μ OR-G_i and β_2 AR-G_s complexes. **a, c**, Interactions between ICL3 of μ OR and G α _i (**a**) and between the cytosolic ends of TM3, TM5 and TM6 of the

μ OR and the α 5-helix of G α _i (**c**). D350 of G α _i is depicted with narrow lines to indicate uncertainty in its position due to poor cryo-EM density for its side chain. **b, d**, The analogous interfaces between β_2 AR and G_s (**b, d**).

The second set of polar contacts involves R263 of μ OR and the backbone carbonyl of I319 on the β 6 strand of $G_{\alpha i}$ (Fig. 5a). Mutations of R263 reduce, but do not abolish, G_i signalling³⁴, which is consistent with the potential importance of stabilizing the β 6 strand of $G_{\alpha i}$ in the observed conformation. There is no analogous interaction in the β_2 AR– G_s complex (Fig. 5b). This additional recognition interface may be necessary for efficient μ OR– G_i coupling owing to the higher affinity for GDP of G_i relative to G_s . Compared to G_s -coupled receptors, additional interactions with the β 6 strand in G_i -coupled receptors may be required to disrupt interactions between the Ras domain and GDP for efficient nucleotide exchange.

The cytosolic ends of μ OR TM3, TM5 and TM6 further stabilize the nucleotide-free conformation of the α 5-helix by interacting with highly conserved residues in the distal C terminus of $G_{\alpha i}$ (Fig. 5c). In particular, C351 (-4 position) of $G_{\alpha i}$ is in close proximity to the cytosolic end of TM3 of μ OR. This cysteine residue has previously been identified as the site of pertussis toxin-mediated inhibition of $G_{i/o}$ family proteins by enzymatic ADP ribosylation³⁵. The close apposition of C351 to the cytoplasmic surface of μ OR highlights how the addition of a bulky modification at this position can completely inhibit receptor coupling and nucleotide exchange³⁵. In addition to this interaction, μ OR residues M255^{5,61}, I278^{6,33}, M281^{6,36} and V282^{6,37} form a hydrophobic pocket that engages the absolutely conserved $G_{\alpha i}$ residue L353 (-2 position) in the α 5-helix. M255^{5,61} and M281^{6,36} have previously been observed in NMR experiments to respond to activation by DAMGO³⁶, suggesting that this region undergoes conformational changes prior to G-protein coupling. Further stabilization, however, is likely to be provided by a hydrogen bond between R277^{6,32} and the backbone carbonyl of L353 (Fig. 5b). Notably, interactions between the C terminus of the α 5-helix and the receptor core are entirely different in the β_2 AR– G_s complex (Fig. 5d).

Our findings provide structural insights into why μ OR does not couple to G_s , but do not explain the mechanism of G-protein-coupling specificity across all GPCRs. It is possible that coupling specificity is determined at an intermediate step in the formation of a GPCR–G-protein complex, such as the initial interactions between the GDP-bound G protein and the agonist-bound receptor. Recent single molecule fluorescence studies provide evidence for a transient intermediate complex between GDP-bound G_s and the β_2 AR that is associated with a smaller outward movement of TM6³⁷. Previous studies suggest that amino acids C-terminal to helix 8 confer coupling specificity for G_q in the M_3 muscarinic receptor (M_3R)³⁸. Given that there are no interactions between the C termini of the β_2 AR or μ OR and their respective G proteins in the nucleotide-free complexes, we hypothesize that engagement of G_q with the C terminus of M_3R may occur at an earlier stage in complex formation. Thus, the nucleotide-free GPCR–G-protein complex may be preceded by one or more GDP-bound intermediates characterized by dynamic low-affinity interactions with the receptor. Such ‘initial encounter’ complexes may show larger energetic differences among interactions with various G-protein subtypes than the nucleotide-free state, and would thereby contribute more critically to coupling specificity. The transient nature of such interactions, however, poses challenges for structure determination by crystallography or cryo-EM.

Online content

Any Methods, including any statements of data availability and Nature Research reporting summaries, along with any additional references and Source Data files, are available in the online version of the paper at <https://doi.org/10.1038/s41586-018-0219-7>.

Received: 31 December 2017; Accepted: 4 May 2018;

Published online 13 June 2018.

- Matthes, H. W. et al. Loss of morphine-induced analgesia, reward effect and withdrawal symptoms in mice lacking the mu-opioid-receptor gene. *Nature* **383**, 819–823 (1996).
- Barnett, M. L., Olenski, A. R. & Jena, A. B. Opioid-prescribing patterns of emergency physicians and risk of long-term use. *N. Engl. J. Med.* **376**, 663–673 (2017).

- Connor, M. & Christie, M. D. Opioid receptor signalling mechanisms. *Clin. Exp. Pharmacol. Physiol.* **26**, 493–499 (1999).
- Raffa, R. B., Martinez, R. P. & Connely, C. D. G-protein antisense oligodeoxyribonucleotides and μ -opioid supraspinal antinociception. *Eur. J. Pharmacol.* **258**, R5–R7 (1994).
- Raehal, K. M., Walker, J. K. L. & Bohn, L. M. Morphine side effects in β -arrestin 2 knockout mice. *J. Pharmacol. Exp. Ther.* **314**, 1195–1201 (2005).
- Schmid, C. L. et al. Bias factor and therapeutic window correlate to predict safer opioid analgesics. *Cell* **171**, 1165–1175.e13 (2017).
- DeWire, S. M. et al. A G protein-biased ligand at the μ -opioid receptor is potently analgesic with reduced gastrointestinal and respiratory dysfunction compared with morphine. *J. Pharmacol. Exp. Ther.* **344**, 708–717 (2013).
- Manglik, A. et al. Structure-based discovery of opioid analgesics with reduced side effects. *Nature* **537**, 185–190 (2016).
- Rasmussen, S. G. F. et al. Crystal structure of the β 2 adrenergic receptor-Gs protein complex. *Nature* **477**, 549–555 (2011).
- Zhang, Y. et al. Cryo-EM structure of the activated GLP-1 receptor in complex with a G protein. *Nature* **546**, 248–253 (2017).
- Liang, Y.-L. et al. Phase-plate cryo-EM structure of a class B GPCR–G-protein complex. *Nature* **546**, 118–123 (2017).
- Huang, W. et al. Structural insights into μ -opioid receptor activation. *Nature* **524**, 315–321 (2015).
- Ballesteros, J. A. & Weinstein, H. in *Receptor Molecular Biology* Vol. 25 (ed. Sealfon, S. C.) Ch. 19 (Elsevier, 1995).
- Manglik, A. et al. Crystal structure of the μ -opioid receptor bound to a morphinan antagonist. *Nature* **485**, 321–326 (2012).
- Granier, S. et al. Structure of the δ -opioid receptor bound to naltrindole. *Nature* **485**, 400–404 (2012).
- Wu, H. et al. Structure of the human κ -opioid receptor in complex with JDTic. *Nature* **485**, 327–332 (2012).
- Che, T. et al. Structure of the nanobody-stabilized active state of the kappa opioid receptor. *Cell* **172**, 55–67.e15 (2018).
- Fenalti, G. et al. Structural basis for bifunctional peptide recognition at human δ -opioid receptor. *Nat. Struct. Mol. Biol.* **22**, 265–268 (2015).
- Emmerson, P. J., Liu, M. R., Woods, J. H. & Medzihradsky, F. Binding affinity and selectivity of opioids at mu, delta and kappa receptors in monkey brain membranes. *J. Pharmacol. Exp. Ther.* **271**, 1630–1637 (1994).
- Minami, M. et al. DAMGO, a μ -opioid receptor selective ligand, distinguishes between μ - and κ -opioid receptors at a different region from that for the distinction between μ - and δ -opioid receptors. *FEBS Lett.* **364**, 23–27 (1995).
- DiMaio, J. & Schiller, P. W. A cyclic enkephalin analog with high in vitro opiate activity. *Proc. Natl. Acad. Sci. USA* **77**, 7162–7166 (1980).
- Rasmussen, S. G. F. et al. Structure of a nanobody-stabilized active state of the β 2 adrenoceptor. *Nature* **469**, 175–180 (2011).
- Wall, M. A. et al. The structure of the G protein heterotrimer $G_{\alpha 1}\beta_1\gamma_2$. *Cell* **83**, 1047–1058 (1995).
- Dror, R. O. et al. Signal transduction. Structural basis for nucleotide exchange in heterotrimeric G proteins. *Science* **348**, 1361–1365 (2015).
- Van Eps, N. et al. Interaction of a G protein with an activated receptor opens the interdomain interface in the alpha subunit. *Proc. Natl. Acad. Sci. USA* **108**, 9420–9424 (2011).
- Kaya, A. I. et al. A conserved phenylalanine as a relay between the α 5 helix and the GDP binding region of heterotrimeric G protein α subunit. *J. Biol. Chem.* **289**, 24475–24487 (2014).
- Chung, K. Y. et al. Conformational changes in the G protein G_s induced by the β_2 adrenergic receptor. *Nature* **477**, 611–615 (2011).
- Choe, H. W. et al. Crystal structure of metarhodopsin II. *Nature* **471**, 651–655 (2011).
- Conklin, B. R., Farfel, Z., Lustig, K. D., Julius, D. & Bourne, H. R. Substitution of three amino acids switches receptor specificity of $G_q\alpha$ to that of $G_{\alpha i}$. *Nature* **363**, 274–276 (1993).
- Isberg, V. et al. Generic GPCR residue numbers—aligning topology maps while minding the gaps. *Trends Pharmacol. Sci.* **36**, 22–31 (2015).
- Isberg, V. et al. GPCRdb: an information system for G protein-coupled receptors. *Nucleic Acids Res.* **42**, D422–D425 (2014).
- Ravindranathan, A. et al. Functional characterization of human variants of the mu-opioid receptor gene. *Proc. Natl. Acad. Sci. USA* **106**, 10811–10816 (2009).
- Skorpen, F. et al. The rare Arg181Cys mutation in the μ opioid receptor can abolish opioid responses. *Acta Anaesthetol. Scand.* **60**, 1084–1091 (2016).
- Chapatiuk, V., Loh, H. H. & Law, P. Y. Ligand-selective activation of μ -opioid receptor: demonstrated with deletion and single amino acid mutations of third intracellular loop domain. *J. Pharmacol. Exp. Ther.* **305**, 909–918 (2003).
- West, R. E., Moss, J., Vaughan, M., Liu, T. & Liu, T. Y. Pertussis toxin-catalyzed ADP-ribosylation of transducin. Cysteine 347 is the ADP-ribose acceptor site. *J. Biol. Chem.* **260**, 14428–14430 (1985).
- Okude, J. et al. Identification of a conformational equilibrium that determines the efficacy and functional selectivity of the μ -opioid receptor. *Angew. Chem. Int. Edn Engl.* **54**, 15771–15776 (2015).
- Gregorio, G. G. et al. Single-molecule analysis of ligand efficacy in β_2 AR–G-protein activation. *Nature* **547**, 68–73 (2017).
- Qin, K., Dong, C., Wu, G. & Lambert, N. A. Inactive-state preassembly of G_q -coupled receptors and G_q heterotrimers. *Nat. Chem. Biol.* **7**, 740–747 (2011).

Acknowledgements We thank J.-P. Carralot (F. Hoffmann–La Roche) for help in antibody generation, C. Yoshioka and C. Lopez for assistance with data collection, M. Siegrist, G. Schmid, B. Rutten, D. Zulau, S. Kueng (Roche Non-Clinical Biorepository) and R. Thoma for technical assistance with biomass

and cell line generation. We also acknowledge N. Moriarty (Lawrence Berkeley National Laboratories) for help with generation of parameters for DAMGO and general advice for refinement of our model. The work is supported by NIH grant R37DA036246 (B.K.K., S.G. and G.S.) and NIH grant RO1GM083118 (B.K.K.). Research reported in this publication was supported by the National Institute of General Medical Sciences of the National Institutes of Health under award number T32GM007276 (A.K.). The content is solely the responsibility of the authors and does not necessarily represent the official view of the National Institutes of Health. S.M. was supported by the Roche Postdoctoral Fellowship (RPF ID: 113). G.F.X.S. acknowledges the Swiss National Science Foundation for grants 310030_153145 and 310030B_17335 and long-term financial support from the Paul Scherrer Institute. B.K.K. is a Chan-Zuckerberg Biohub Investigator.

Reviewer information *Nature* thanks L. Shi, D. Wacker and the other anonymous reviewer(s) for their contribution to the peer review of this work.

Author contributions A.K. prepared the μ OR–G_i complex and refined the structure from cryo-EM density maps. H.H. obtained and processed cryo-EM data with the assistance of Y.Z. and Q.Q. S.M. identified and prepared scFv16

with assistance from R.D. and H.M and under supervision of G.F.X.S. A.M., D.H. S.G. and A.K. developed the procedure for forming the μ OR–G_i complex. N.R.L and J.M.P performed molecular dynamics simulations under supervision of R.O.D. W.I.W. aided in map interpretation and model refinement. A.K., A.M., B.K.K. and G.S. wrote the manuscript. A.M., G.S. and B.K.K. supervised the project.

Competing interests B.K. is a founder of and consultant for ConfometRx.

Additional information

Extended data is available for this paper at <https://doi.org/10.1038/s41586-018-0219-7>.

Supplementary information is available for this paper at <https://doi.org/10.1038/s41586-018-0219-7>.

Reprints and permissions information is available at <http://www.nature.com/reprints>.

Correspondence and requests for materials should be addressed to A.M. or G.S. or B.K.K.

Publisher's note: Springer Nature remains neutral with regard to jurisdictional claims in published maps and institutional affiliations.

METHODS

No statistical methods were used to predetermine sample size. The experiments were not randomized and the investigators were not blinded to allocation during experiments and outcome assessment.

Purification of μOR. These studies utilized a previously described mouse μOR construct with cleavable N- and C-terminal domains¹². In brief, the receptor was expressed in *Spodoptera frugiperda* Sf9 insect cells using the baculovirus method (Expression Systems), extracted from insect cell membranes with *n*-dodecyl-β-D-maltoside (DDM, Antrace), and purified by nickel-chelating sepharose chromatography. The Ni-NTA eluate was loaded onto M1 anti-Flag immunoaffinity resin and washed with progressively lower concentrations of the antagonist naloxone. The μOR was then eluted in a buffer consisting of 20 mM Hepes pH 7.5, 100 mM NaCl, 0.1% DDM and 0.01% cholesterol hemisuccinate (CHS) supplemented with 50 nM naloxone, Flag peptide and 5 mM EDTA. The monomeric fraction was purified by size exclusion chromatography on a Superdex 200 10/300 gel filtration column (GE Healthcare) in 20 mM Hepes pH 7.5, 100 mM NaCl, 0.1% DDM, 0.01% CHS, and 1 μM DAMGO. A further twofold molar excess of DAMGO was added to the preparation and the resulting agonist-bound μOR preparation was concentrated to ~100 μM.

Expression and purification of heterotrimeric G_i. Heterotrimeric G_i was expressed and purified as previously described²⁴. In brief, *Trichoplusia ni* Hi5 insect cells were co-infected with two viruses, one encoding the wild-type human Gα_i subunit and another encoding the wild-type human β₁γ₂ subunits with an octahistidine tag inserted at the amino terminus of the β₁ subunit. Cultures were harvested 48 h post infection. Cells were lysed in hypotonic buffer and lipid-modified heterotrimeric G_i was extracted in a buffer containing 1% sodium cholate. The soluble fraction was purified using Ni-NTA chromatography, and the detergent was exchanged from cholate to DDM on a column. After elution, the protein was dialyzed against a buffer containing 20 mM Hepes pH 7.5, 100 mM NaCl, 0.015% DDM, 100 μM TCEP, 10 μM GDP, and concentrated to ~20 mg/ml for further complexing with the μOR.

Generation of scFv16. Six to eight week old female Balb/c mice were immunized with a purified rhodopsin-G_i complex³⁹. Hybridoma cells were prepared using splenocytes of immunized mice using standard methods in combination with PAI myeloma cells (RRID: CVCL J288). Clones that showed a positive reaction to purified rhodopsin(N2C/D282C/M257Y)-G_i complex in an ELISA assay and by immunoprecipitation were further characterized as monoclonal antibodies or Fab fragments. Fab-16 was selected from the initial pool of clones because it prevented dissociation of the rhodopsin(N2C/D282C/M257Y)-G_i complex by GTPγS, and therefore acted as a stabilizing chaperone in the same manner as Nb35 for G_s. The full sequences of constructs used are listed in Supplementary Fig. 1. All animal studies were performed at Roche Innovation Center in Basel according to ethical guidelines and internal IRB approval. All cell lines were obtained from the manufacturer and tested for contamination.

A C-terminal hexahistidine-tagged single chain construct of Fab16 (scFv16) was cloned into a modified pVL1392 vector containing a GP67 secretion signal immediately prior to the amino terminus of the scFv, expressed in secreted form from *Trichoplusia ni* Hi5 insect cells using the baculovirus method, and purified by Ni-NTA chromatography. Supernatant from baculovirus-infected cells was pH balanced by addition of Tris pH 8.0. Chelating agents were quenched by addition of 1 mM nickel chloride and 5 mM calcium chloride and incubation with stirring for 1 h at 25 °C. Resulting precipitates were removed by centrifugation and the supernatant was loaded onto Ni-NTA resin. The column was washed with 20 mM Hepes pH 7.5, 500 mM NaCl, and 10 mM imidazole followed by a low salt wash comprised of the same buffer substituted with 100 mM NaCl. Following elution with the same buffer supplemented with 250 mM imidazole, the C-terminal hexahistidine tag was cleaved by incubation with human rhinovirus 3C protease, and the protein was dialyzed into a buffer consisting of 20 mM Hepes pH 7.5 and 100 mM NaCl. Cleaved scFv16 was further purified by reloading over Ni-NTA resin. The flow-through was collected and purified over gel filtration chromatography using a Superdex 200 16/60 column. Monomeric fractions were pooled, concentrated, and flash frozen in liquid nitrogen until further use.

Formation and purification of the μOR-G_i-scFv16 complex. Purified DAMGO-bound μOR was mixed with a 1.2 molar excess of G_i heterotrimer. The coupling reaction was allowed to proceed at 24 °C for 1 h and was followed by addition of apyrase to catalyze hydrolysis of unbound GDP, which destabilizes the nucleotide-free complex⁴⁰. After one more hour at 25 °C, a fourfold volume of 20 mM Hepes pH 7.5, 100 mM NaCl, 1% lauryl maltose neopentyl glycol (L-MNG), 0.1% CHS was added to the complexing reaction to initiate detergent exchange. After 1 h incubation at 25 °C to allow micelle exchange, 1 mM MnCl₂ and lambda phosphatase (New England Biolabs) were added to dephosphorylate the preparation. This reaction was further incubated at 4 °C for 2 h. To remove excess G protein and residual DDM, the complexing mixture was purified by M1 anti-Flag affinity chromatography. Bound complex was first washed in a buffer containing 1%

L-MNG, followed by washes in gradually decreasing L-MNG concentrations. The complex was then eluted in 20 mM Hepes pH 7.5, 100 mM NaCl, 0.01% L-MNG, 0.001% CHS, 300 nM DAMGO, 5 mM EDTA and Flag peptide. The eluted complex was supplemented with 100 μM TCEP to provide a reducing environment. The tobacco etch virus (TEV) protease and human rhinovirus 3C protease were added to cleave the flexible μOR N and C termini. Finally, a 1.2 molar excess of scFv16 was added to the preparation. Once cleavage of the termini was confirmed by SDS-PAGE, the μOR-G_i-scFv16 complex was purified by size exclusion chromatography on a Superdex 200 10/300 column in 20 mM Hepes pH 7.5, 100 mM NaCl, 300 nM DAMGO, 0.00075% L-MNG and 0.00025% glyco-diosgenin (GDN) with 0.0001% CHS total. Peak fractions were concentrated to ~7 mg/ml for electron microscopy studies.

Cryo-EM and 3D reconstructions of μOR-G_i-scFv16 complex. Three microlitres of purified μOR-G_i-scFv16 complex was applied to glow-discharged 200-mesh grids (Quantifoil R1.2/1.3) and subsequently vitrified using a Vitrobot Mark IV (Thermo Fischer Scientific). Cryo-EM imaging was performed on a Titan Krios operated at 300 kV at a nominal magnification of 130,000× using a Gatan K2 Summit direct electron camera in counted mode, corresponding to a pixel size of 1.04 Å. A total of 2642 image stacks were obtained with a defocus range of −0.8 to −2.6 μm. Each stack movie was recorded for a total of 8 s with 0.1 s per frame. The dose rate was 5 e[−]/Å²/s, resulting in an accumulated dose of 40 electrons per Å².

Dose-fractionated image stacks were subjected to beam-induced motion correction using MotionCor2⁴¹. A sum of all frames, filtered according to exposure dose, in each image stack was used for further processing. CTF parameters for each micrograph were determined by Gctf v1.06⁴². Particle selection, two-dimensional and three-dimensional classification, and 3D reconstruction were performed using RELION2.1⁴³, apart from the last round of local refinement and reconstruction that was performed with Frealign⁴⁴. Semi-automated selected 893,426 particle projections were subjected to reference-free 2D classification and averaging using a binned dataset with a pixel size of 2.08 Å. Particles (379,373) with well-defined averages were subjected to further processing. An ab initio map generated by VIPER⁴⁵ was used as initial reference model for maximum-likelihood-based 3D classification, which, however, did not produce classes with notable differences. Thus, all 379,373 particle projections were subjected to 3D refinement, producing a map at 4.3 Å resolution. The dataset was further reduced by removing particle projections from micrographs with resolution lower than 4.5 Å, resulting in a dataset of 359,406 particles that were subjected to refinement and reconstruction after subtracting densities for the mobile Gα α-helical domain and the detergent micelle¹¹. Particle projection assignments from RELION were imported into Frealign⁴⁶ for a final round of local refinement and reconstruction. To prevent overfitting, the resolution limit for each alignment iteration never exceeded the 0.9 value of the Frealign calculated Fourier shell correlation (FSC). The map was further improved after additionally subtracting densities corresponding to the ScFv from the raw particle projections¹¹. The indicated resolution, using Phenix ‘gold standard’ FSC⁴⁷, of the final reconstruction is 3.5 Å and 3.6 Å at FSC 0.143 for the ScFv-subtracted map and the ScFv-including map, respectively. Local resolution was determined using the Bsoft package⁴⁸ with unfiltered half maps as input.

Model building and refinement. The building of a full atomic model for the μOR-G_i complex was aided by the quality and resolution of our map, as well as the existence of high-resolution crystal structures of each of the components that make up the complex. A composite model was formed by rigid body fitting of the active-state μOR (PDB code 5C1M)¹² with nanobody removed, as well as the Ras domain and βγ subunits of GDP-bound G_i (PDB 1GP2)²³. The α5-helix of Gα_i was removed and manually fitted to the density, and the final eight residues that were missing from the extreme C terminus of the 1GP2 structure were manually built in Coot⁴⁹. This starting model was then subjected to iterative rounds of automated refinement in Rosetta⁵⁰ and Phenix real space refine⁴⁷, and manual building in Coot⁴⁹. In the regions of the model for which side-chain density was too weak to unambiguously assign a conformation, we stubbed residues to their C_β position, while preserving sequence information (Supplementary Fig. 2, 3). The final model was visually inspected for general fit to the map, and geometry was further evaluated using Molprobity⁵¹ as part of the Phenix suite of software. Initial restraints for DAMGO were generated using the PRODRG server⁵². To further refine the pose of DAMGO, we chose a pose from molecular dynamics simulation consistent with our map and then performed a refinement using Phenix. This involved manually editing the residue and atom names from a CHARMM parameter file to match the three-letter codes and atom names from the RCSB. In particular, DAL for D-alanine, MEA for N-methyl phenylalanine, and ETA for Gly-ol C terminus. Additional, custom, restraints were generated to maintain planarity of the final peptide bond between MEA and ETA as a supplement to the natural library of Phenix amino acid restraints. Model overfitting was evaluated through its refinement against one cryo-EM half map after randomly displacing all atoms by 0.2 Å. FSC curves were calculated between the resulting model and the half map used for refinement (red curve, Extended Data Fig. 3b, c), as well as between the resulting

model and the other half map for cross validation (green curve, Extended Data Fig. 3b, c), and also against the full map (black curve, Extended Data Fig. 3b, c). The final refinement statistics for both models are provided in Extended Data Table 1.

System setup for molecular dynamics simulations. Molecular dynamics simulations were initiated from an earlier refinement of the structure reported in this study after removing the G protein and ScFv fragment. Prior to beginning simulations, Schrödinger Glide⁵³ was used to relax DAMGO to an energetically favourable conformation. The initial DAMGO pose is depicted in Extended Data Fig. 3. We performed five independent simulations, for each of which initial atom velocities were assigned randomly and independently. Prime (Schrödinger) was used to model missing side chains, and neutral acetyl and methylamide groups were added to cap protein termini. Titratable residues remained in their dominant protonation state at pH 7, as determined using PropKa, except for D^{2.50} and D^{3.49}, which were protonated. Our simulations incorporated the waters from the 5C1M crystal structure.

The prepared protein structures were aligned to the ‘orientation of proteins in membranes’ (OPM) structure for PDB entry 5C1M⁵⁴. The aligned structures were then inserted into a pre-equilibrated palmitoyl-oleoyl-phosphatidylcholine (POPC) bilayer using Dabble, a simulation preparation software⁵⁵. Sodium and chloride ions were added to neutralize each system at a concentration of approximately 150 mM. Bilayer dimensions were chosen to maintain at least a 30 Å buffer between protein images in the *x*-*y* plane and a 20 Å buffer between protein images in the *z* direction. Final system dimensions were approximately 80 × 75 × 90 Å³. Simulation times for each replicate were approximately 1 μs.

Molecular dynamics simulation protocols. We used the CHARMM36m force field for proteins, lipids and ions and the TIP3P model for waters^{56–60}. Parameters for the non-canonical residues in DAMGO were determined by analogy to N-methyl glycine for assigning N-methyl parameters to N-methyl phenylalanine (residue 4) and by analogy to serine to assign parameters to the Gly-ol capping group (residue 5). CMAP terms for D-alanine were inverted from those for L-Alanine to account for the inverted chirality of the residue.

We performed the simulations using the Compute Unified Device Architecture (CUDA) version of Particle-Mesh Ewald Molecular Dynamics (PMEMD) in AMBER on one or two graphical processing units (GPUs)⁶¹. Simulations were performed using the AMBER16⁶² software. Three rounds of minimization were performed, each consisting of 500 iterations of steepest descent minimization, followed by 500 iterations of conjugate gradient descent minimization, with harmonic restraints of 10.0, 5.0 and 1.0 kcal mol⁻¹ Å⁻² placed on the protein and lipids. Systems were heated from 0 K to 100 K in the NVT ensemble over 12.5 ps and then from 100 K to 310 K in the NPT ensemble over 125 ps, using 10.0 kcal mol⁻¹ Å⁻² harmonic restraints applied to lipid and protein heavy atoms. Systems were then equilibrated at 310 K in the NPT ensemble at 1 bar, with harmonic restraints on all protein heavy atoms tapered off by 1.0 kcal mol⁻¹ Å⁻² starting at 5.0 kcal mol⁻¹ Å⁻² in a stepwise fashion every 2 ns for 10 ns and then by 0.1 kcal mol⁻¹ Å⁻² in a stepwise fashion every 2 ns for 20 ns. Production simulations were performed in the NPT ensemble at 310 K and 1 bar, using a Langevin thermostat for temperature coupling and a Monte Carlo barostat for pressure coupling. These simulations used a 4-fs time step with hydrogen mass repartitioning⁶³. Bond lengths to hydrogen atoms were constrained using SHAKE. Simulations used periodic boundary conditions. Non-bonded interactions were cut off at 9.0 Å, and long-range electrostatic interactions were computed using Particle Mesh Ewald (PME) with an Ewald coefficient of approximately 0.31 Å and an interpolation order of four. The FFT grid size was chosen such that the width of a grid cell was approximately 1 Å.

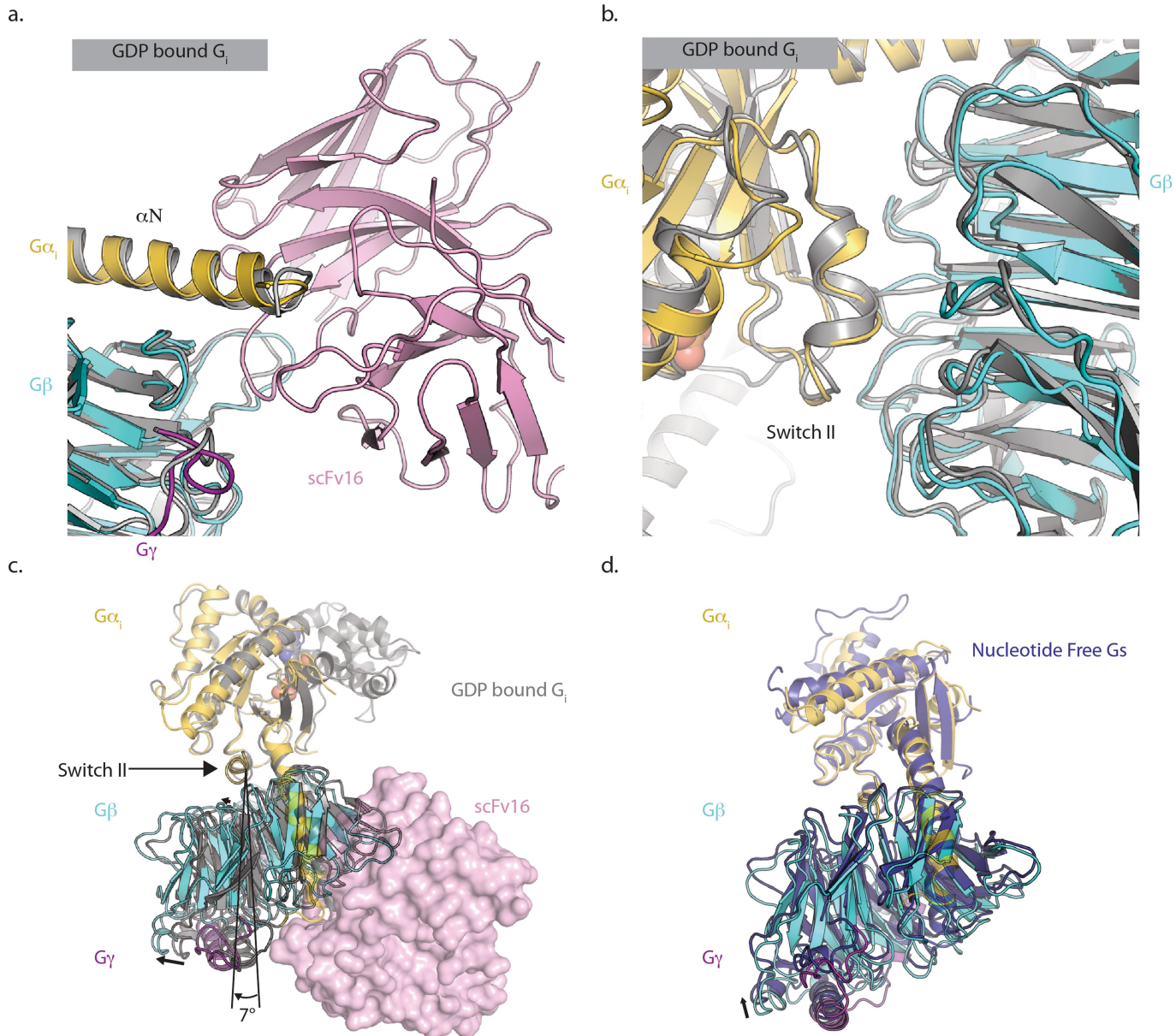
During production simulations, all residues within 5 Å of the G-protein interface were restrained to the initial structure using 5.0 kcal mol⁻¹ Å⁻² harmonic restraints applied to non-hydrogen atoms. Using such restraints reduces the overall system size, enabling more simulation, while ensuring that the receptor maintains an active conformation throughout the simulation.

Analysis protocols for molecular dynamics simulation. Trajectory snapshots were saved every 200 ps during production simulations. The AmberTools17 CPPTRAJ package was used to reimage and center trajectories⁶⁴. Simulations were visualized and analysed using Visual Molecular Dynamics (VMD)⁶⁵. In two simulations, DAMGO was trapped in an unstable binding pose, wherein the water-mediated interaction between the DAMGO tyrosine residue and H297 failed to form during equilibration, and instead a direct hydrogen bond between these residues was formed. Our analysis is based on the other three simulations, in which DAMGO’s pose was consistent with the cryo-EM density. Water occupancy maps were generated using AmberTools17 GIST^{66,67}. Frames from every 1 ns of simulation, excluding the first 400 ns, aligned to the initial structure, were used as input. The grid size was set to 0.25 Å. The resulting map was smoothed using a Gaussian filter with a standard deviation of two grid cells.

Reporting summary. Further information on experimental design is available in the Nature Research Reporting Summary linked to this paper.

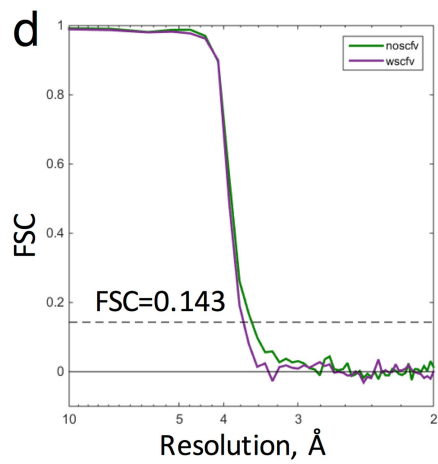
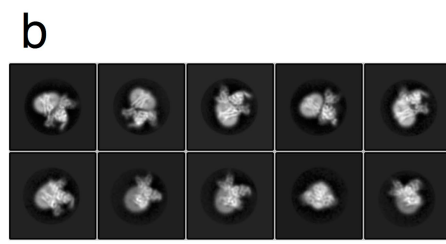
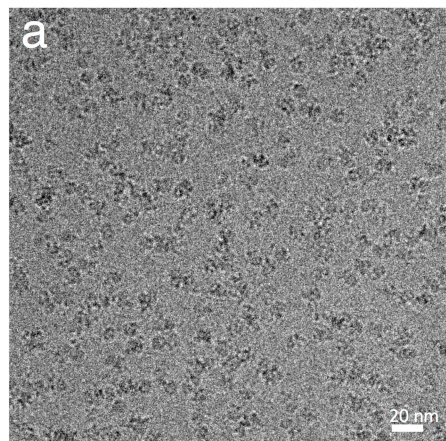
Data availability. All data generated or analysed during this study are included in this published article and its Supplementary Information. Sequences of constructs used in this study are listed in Supplementary Fig. 1. The cryo-EM density maps for the μOR-G_i complex with, and without, scFv16 have been deposited in the Electron Microscopy Data Bank (EMDB) under accession codes EMD-7868 and EMD-7869, respectively. The coordinates for the models of μOR-G_i with, and without, scFv-16 have been deposited in the Protein Data Bank (PDB) under accession numbers 6DDE and 6DDF respectively.

39. Maeda, S. et al. Crystallization scale preparation of a stable GPCR signaling complex between constitutively active rhodopsin and G-protein. *PLoS One* **9**, e98714 (2014).
40. Westfield, G. H. et al. Structural flexibility of the Gαs α-helical domain in the β₂-adrenoceptor Gs complex. *Proc. Natl Acad. Sci. USA* **108**, 16086–16091 (2011).
41. Zheng, S. Q., Palovcak, E., Armache, J.-P., Verba, K. A., Cheng, Y. & Agard, D. A. MotionCor2: anisotropic correction of beam-induced motion for improved cryo-electron microscopy. *Nat. Methods* **14**, 331–332 (2016).
42. Zhang, K. Gctf: Real-time CTF determination and correction. *J. Struct. Biol.* **193**, 1–12 (2016).
43. Scheres, S. H. W. RELION: implementation of a Bayesian approach to cryo-EM structure determination. *J. Struct. Biol.* **180**, 519–530 (2012).
44. Grigorieff, N. FREALIGN: high-resolution refinement of single particle structures. *J. Struct. Biol.* **157**, 117–125 (2007).
45. Penczek, P. A., Grassucci, R. A. & Frank, J. The ribosome at improved resolution: new techniques for merging and orientation refinement in 3D cryo-electron microscopy of biological particles. *Ultramicroscopy* **53**, 251–270 (1994).
46. Grigorieff, N. Frealign: an exploratory tool for single-particle Cryo-EM. *Methods Enzymol.* **579**, 191–226 (2016).
47. Adams, P. D. et al. The Phenix software for automated determination of macromolecular structures. *Methods* **55**, 94–106 (2011).
48. Heymann, J. B. & Belnap, D. M. Bsoft: image processing and molecular modeling for electron microscopy. *J. Struct. Biol.* **157**, 3–18 (2007).
49. Emsley, P. & Cowtan, K. Coot: model-building tools for molecular graphics. *Acta Crystallogr. D* **60**, 2126–2132 (2004).
50. Wang, R. Y.-R. et al. Automated structure refinement of macromolecular assemblies from cryo-EM maps using Rosetta. *eLife* **5**, 352 (2016).
51. Williams, C. J. et al. MolProbity: More and better reference data for improved all-atom structure validation. *Protein Sci.* **27**, 293–315 (2018).
52. Schüttelkopf, A. W. & van Aalten, D. M. F. PRODRG: a tool for high-throughput crystallography of protein-ligand complexes. *Acta Crystallogr. D* **60**, 1355–1363 (2004).
53. Friesner, R. A. et al. Glide: a new approach for rapid, accurate docking and scoring. 1. Method and assessment of docking accuracy. *J. Med. Chem.* **47**, 1739–1749 (2004).
54. Lomize, M. A., Lomize, A. L., Pogozheva, I. D. & Mosberg, H. I. OPM: orientations of proteins in membranes database. *Bioinformatics* **22**, 623–625 (2006).
55. Betz, R. Dibble (v.2.6.3). <https://doi.org/10.5281/zenodo.836914> (2017).
56. Best, R. B., Mittal, J., Feig, M. & MacKerell, A. D. Inclusion of many-body effects in the additive CHARMM protein CMAP potential results in enhanced cooperativity of α-helix and β-hairpin formation. *Biophys. J.* **103**, 1045–1051 (2012).
57. Best, R. B. et al. Optimization of the additive CHARMM all-atom protein force field targeting improved sampling of the backbone φ, ψ and side-chain χ₁ and χ₂ dihedral angles. *J. Chem. Theory Comput.* **8**, 3257–3273 (2012).
58. Huang, J. & MacKerell, A. D. CHARMM36 all-atom additive protein force field: validation based on comparison to NMR data. *J. Comput. Chem.* **34**, 2135–2145 (2013).
59. Klauda, J. B. et al. Update of the CHARMM all-atom additive force field for lipids: validation on six lipid types. *J. Phys. Chem. B* **114**, 7830–7843 (2010).
60. Huang, J. et al. CHARMM36m: an improved force field for folded and intrinsically disordered proteins. *Nat. Methods* **14**, 71–73 (2016).
61. Salomon-Ferrer, R., Götz, A. W., Poole, D., Le Grand, S. & Walker, R. C. Routine microsecond molecular dynamics simulations with AMBER on GPUs. 2. Explicit solvent particle mesh Ewald. *J. Chem. Theory Comput.* **9**, 3878–3888 (2013).
62. Case, D. A. et al. Amber (v.16). <http://ambermd.org> (2018).
63. Hopkins, C. W., Le Grand, S., Walker, R. C. & Roitberg, A. E. Long-time-step molecular dynamics through hydrogen mass repartitioning. *J. Chem. Theory Comput.* **11**, 1864–1874 (2015).
64. Roe, D. R. & Cheatham, T. E. III. PTraj and CPPTRAJ: software for processing and analysis of molecular dynamics trajectory data. *J. Chem. Theory Comput.* **9**, 3084–3095 (2013).
65. Humphrey, W., Dalke, A. & Schulten, K. VMD: visual molecular dynamics. *J. Mol. Graph.* **14**, 33–38 (1996).
66. Nguyen, C. N., Young, T. K. & Gilson, M. K. Grid inhomogeneous solvation theory: hydration structure and thermodynamics of the miniature receptor cucurbit[7]uril. *J. Chem. Phys.* **137**, 044101 (2012).
67. Nguyen, C., Gilson, M. K. & Young, T. Structure and thermodynamics of molecular hydration via grid inhomogeneous solvation theory. Preprint at <https://arXiv.org/abs/1108.4876> (2011).

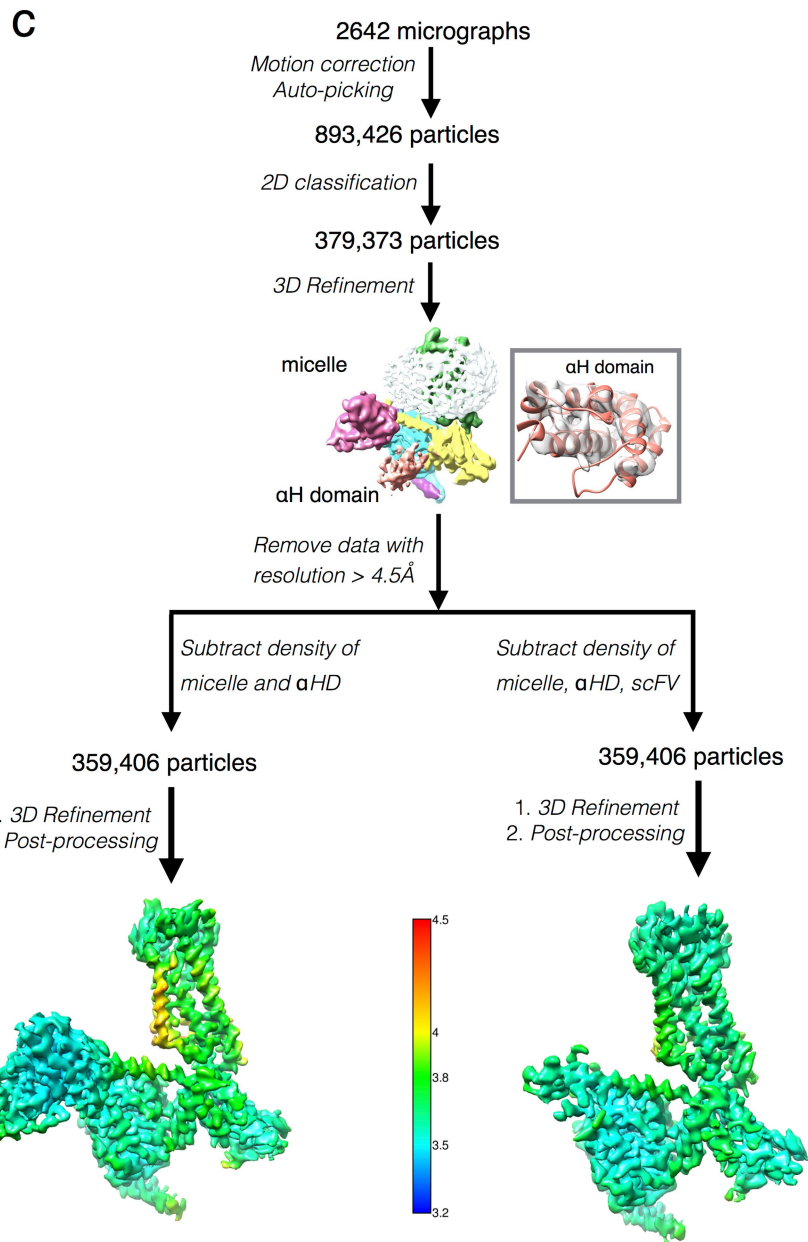


Extended Data Fig. 1 | Binding characteristics of scFv. **a, b,** scFv 16 does not perturb the interfaces between $G\alpha$ and $G\beta$ at its binding epitope (**a**) or the switch II region located ~40 Å away (**b**). Our structure is coloured by chain, whereas the structure of GDP-bound G_{i1} heterotrimer (PDB code 1GP2) is coloured grey. **c,** In the nucleotide-free state (coloured by

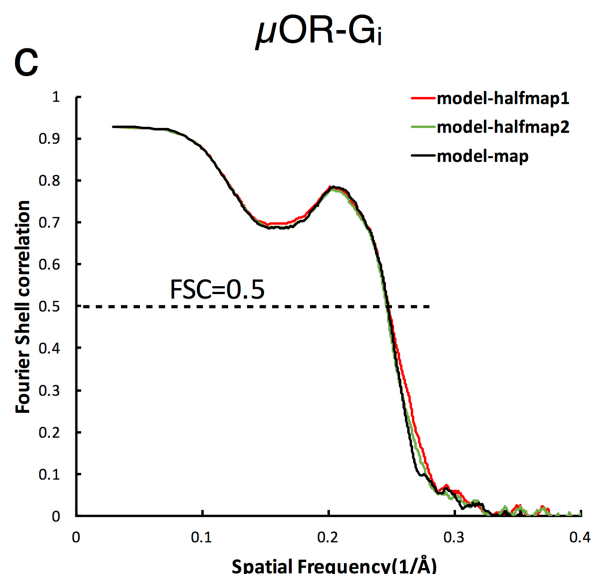
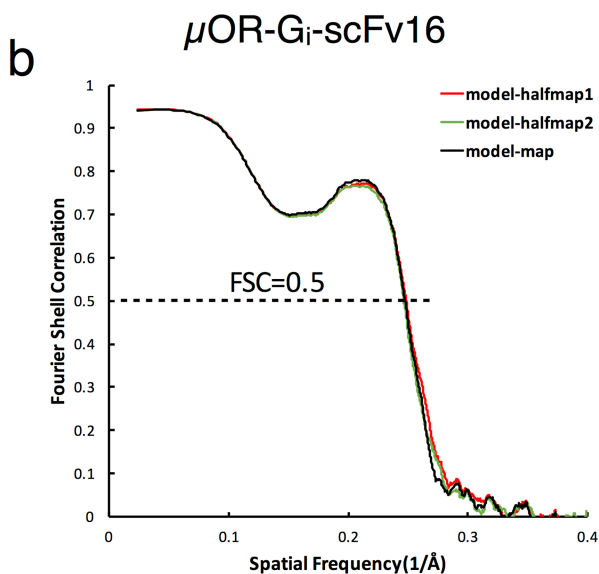
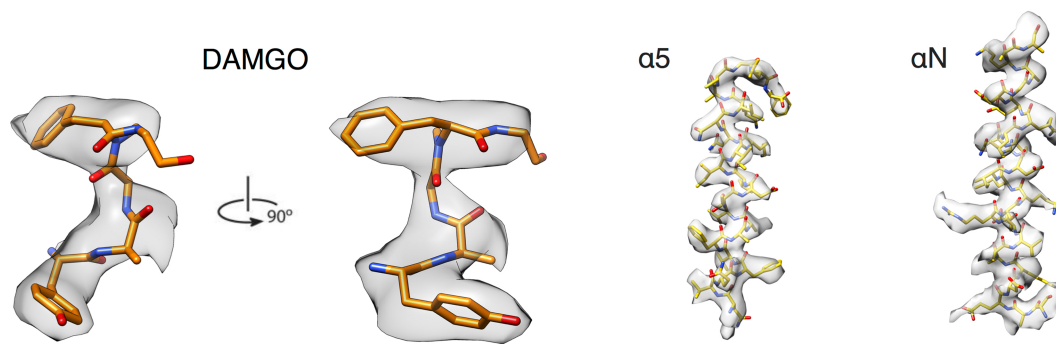
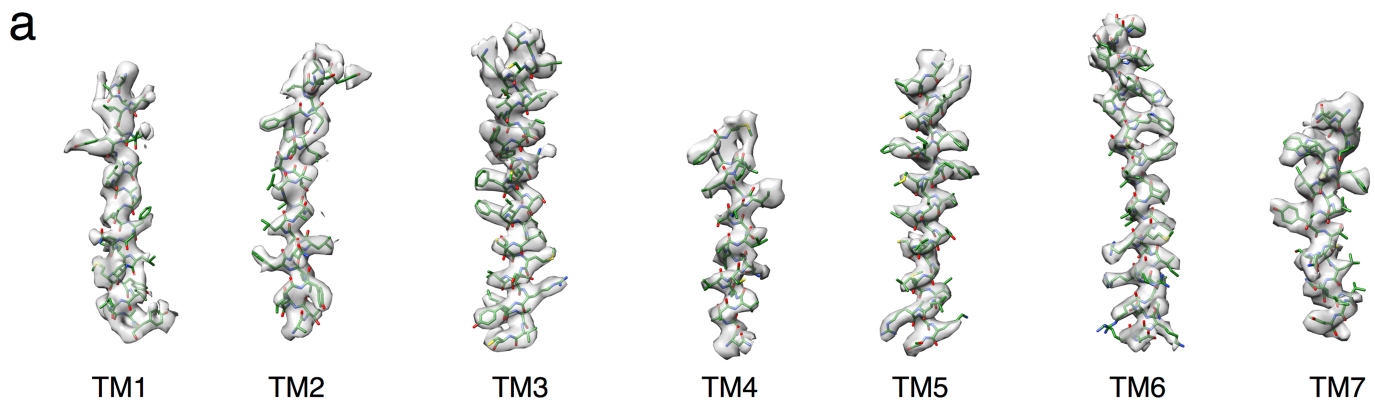
subunit), there is a ~7° rotation of $G\beta\gamma$ relative to the $G\alpha_s$ switch II domain when compared to the GDP-bound form. **d,** This rotated conformation is similar to that observed in nucleotide-free G_s coupled to the β_2 AR (PDB code 3SN6).



Extended Data Fig. 2 | Cryo-EM data processing. **a**, Representative cryo-EM image of the μ OR-G_i complex. Scale bar, 20 nm. **b**, Representative 2D averages showing distinct secondary structure features from different views of the complex. **c**, Flow chart of cryo-EM data processing. The unmasked map in the middle of the chart has been coloured by subunit. The inset shows the fit of the crystal structure of the α -helical domain in the



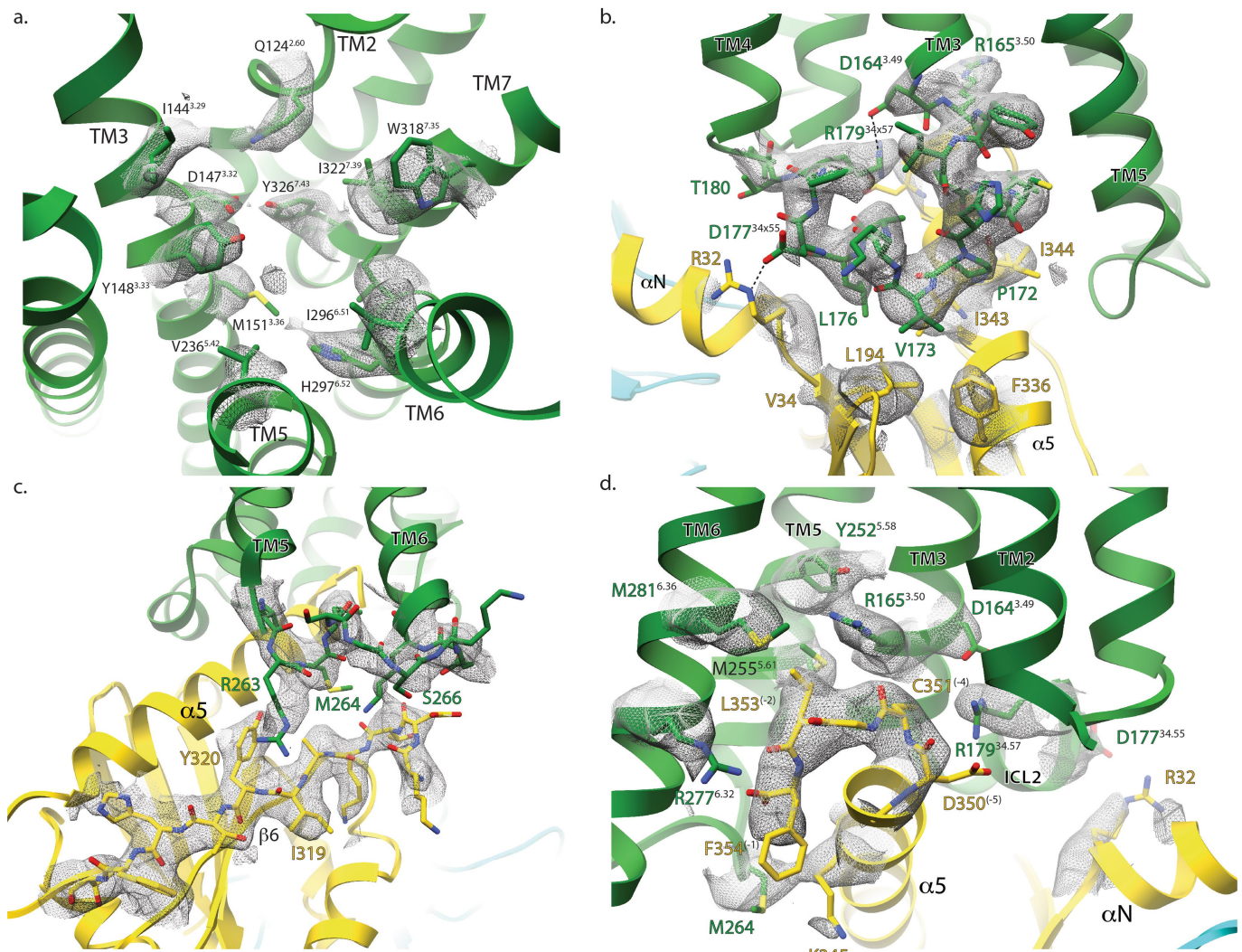
corresponding density of the unmasked reconstruction. 3D density maps coloured according to local resolution. **d**, 'Gold standard' FSC curves from Phenix indicate overall nominal resolutions of 3.5 Å and 3.6 Å using the $\text{FSC} = 0.143$ criterion for the scFv-subtracted map (green curve) and scFv-retained maps (purple curve), respectively.



Extended Data Fig. 3 | Cryo-EM map versus refined structure.

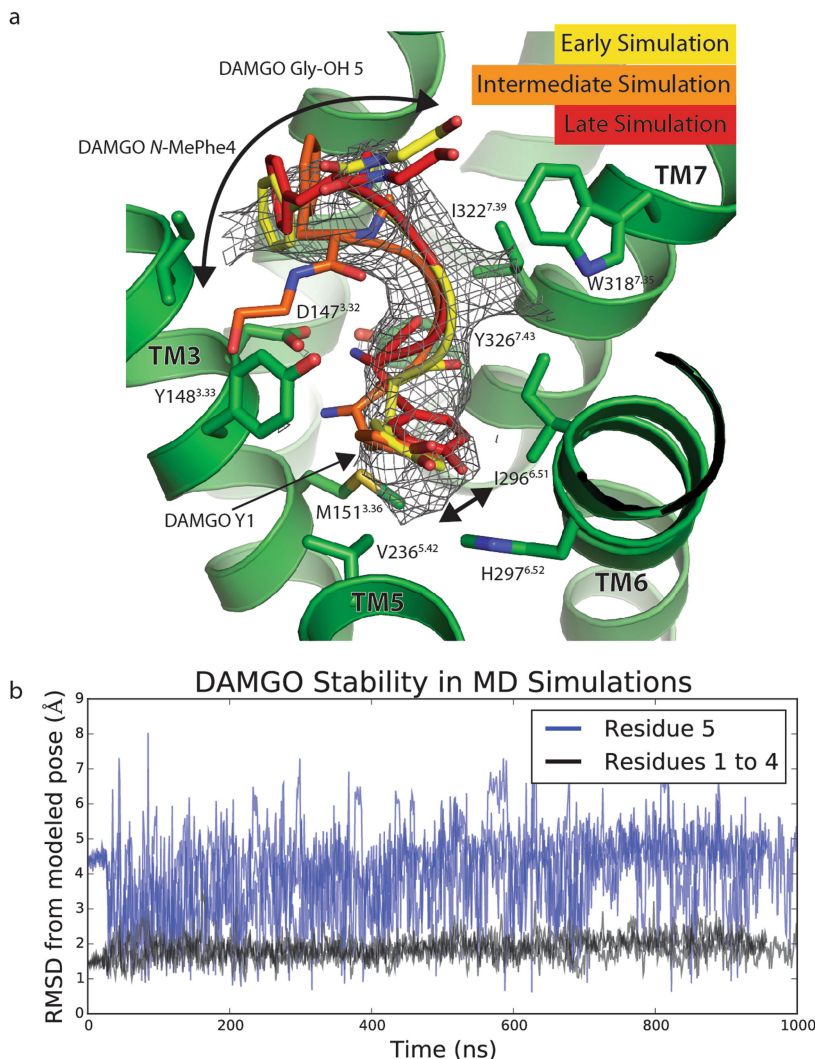
a, Cryo-EM density map (scFv subtracted) and model are shown for all seven transmembrane α -helices of the μOR , DAMGO, and $\text{G}\alpha$ helices $\alpha 5$ and αN . **b, c**, Cross-validation of model to cryo-EM density map. The model was refined against one half map after displacement of atoms by 0.2 \AA , and FSC curves were calculated between this model and the final

cryo-EM map (full dataset, black) of the outcome of model refinement with a half map versus the same map (red), and of the outcome of model refinement with a half map versus the other half map (green). The results of the scFv-retained model versus map (**b**) and of scFv-subtracted model versus map (**c**) are shown.



Extended Data Fig. 4 | Selected cryo-EM densities of μ OR–G α _i complex. **a–d**, Cryo-EM density (displayed as mesh) surrounding residues involved in DAMGO binding (**a**), μ OR–G α _i interaction around ICL2 (**b**), ICL3 (**c**),

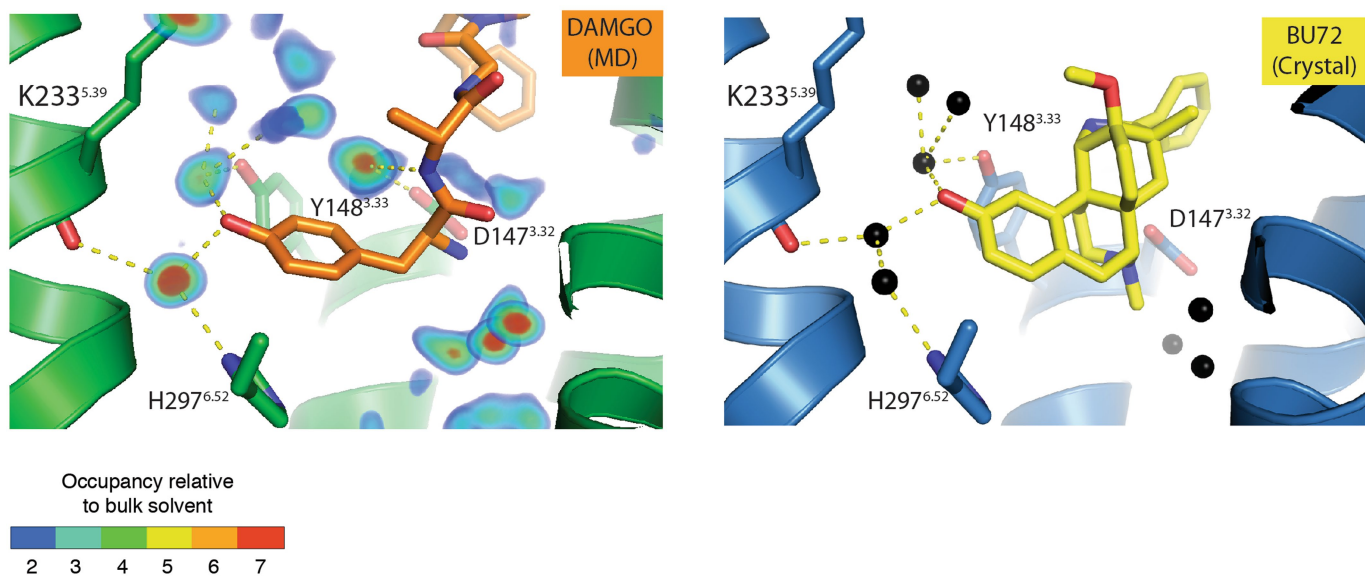
and cytoplasmic ends of the μ OR transmembrane helices (**d**). These figures accompany the models shown in Figs. 1e, 4b, 5a and 5c, respectively.



Extended Data Fig. 5 | Stability of DAMGO in molecular dynamics simulations. **a**, Over the course of molecular dynamics simulations, the positions of the first four residues of DAMGO do not significantly change, while the fifth residue (Gly-ol) shows significant variability in position. Frames from the first and last 100 ns are shown with an intermediate to highlight both the relative stability of the first four amino acids and the flexibility of the fifth. Arrows show the extent of motion in the N- and

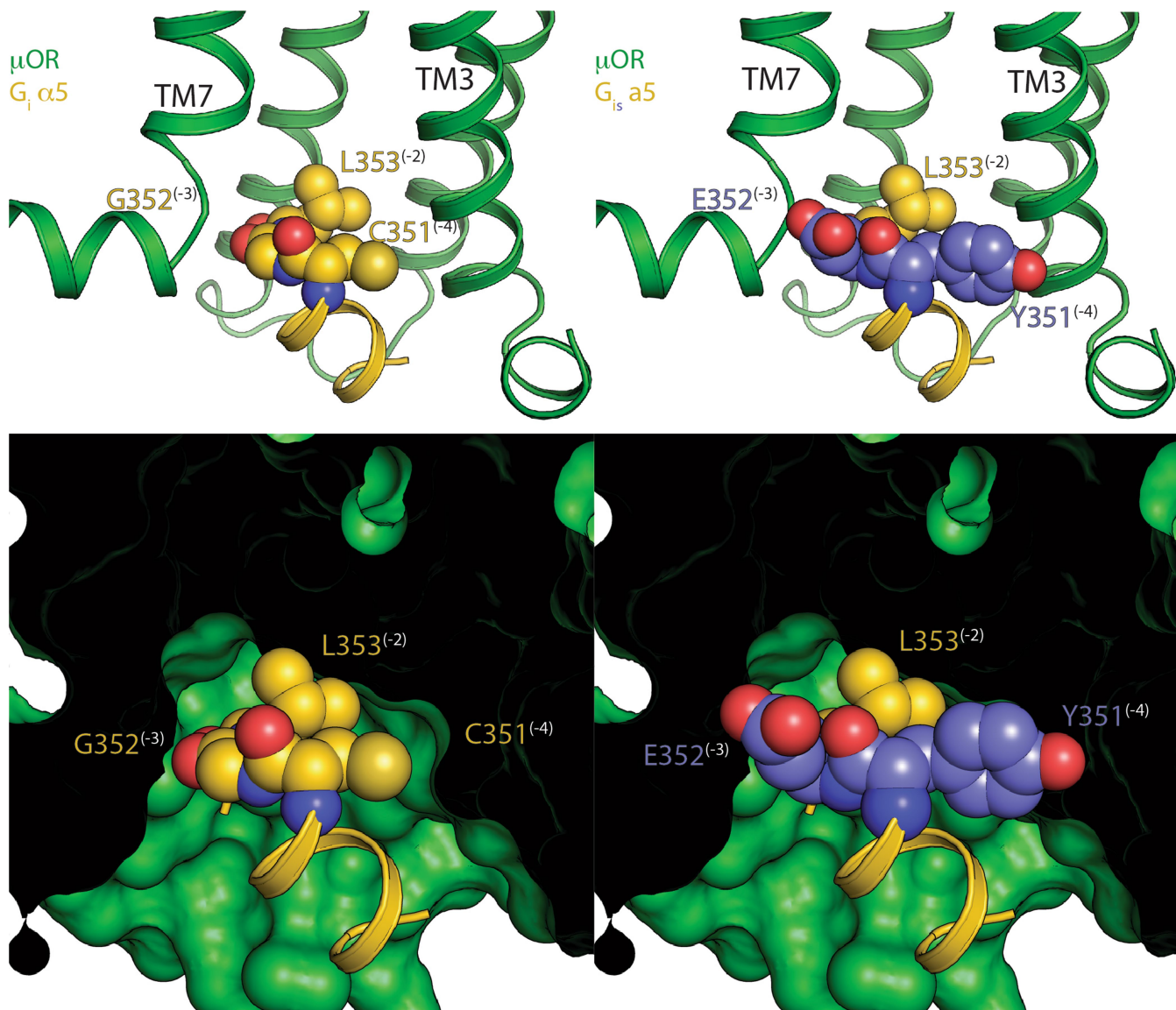
C-terminal residues over the course of simulation. Cryo-EM density for DAMGO is shown as mesh. **b**, Root mean standard deviations (RMSDs) from the modelled pose of DAMGO to the pose during molecular dynamics simulations. The RMSD calculations include heavy atoms on the peptide backbone. Data from three independent simulations are plotted. The RMSDs for residues 1 to 4 (black) and the C-terminal Gly-ol (blue) are plotted separately to highlight their stability and mobility, respectively.

Regions of high water density in the DAMGO binding pocket during MD simulation



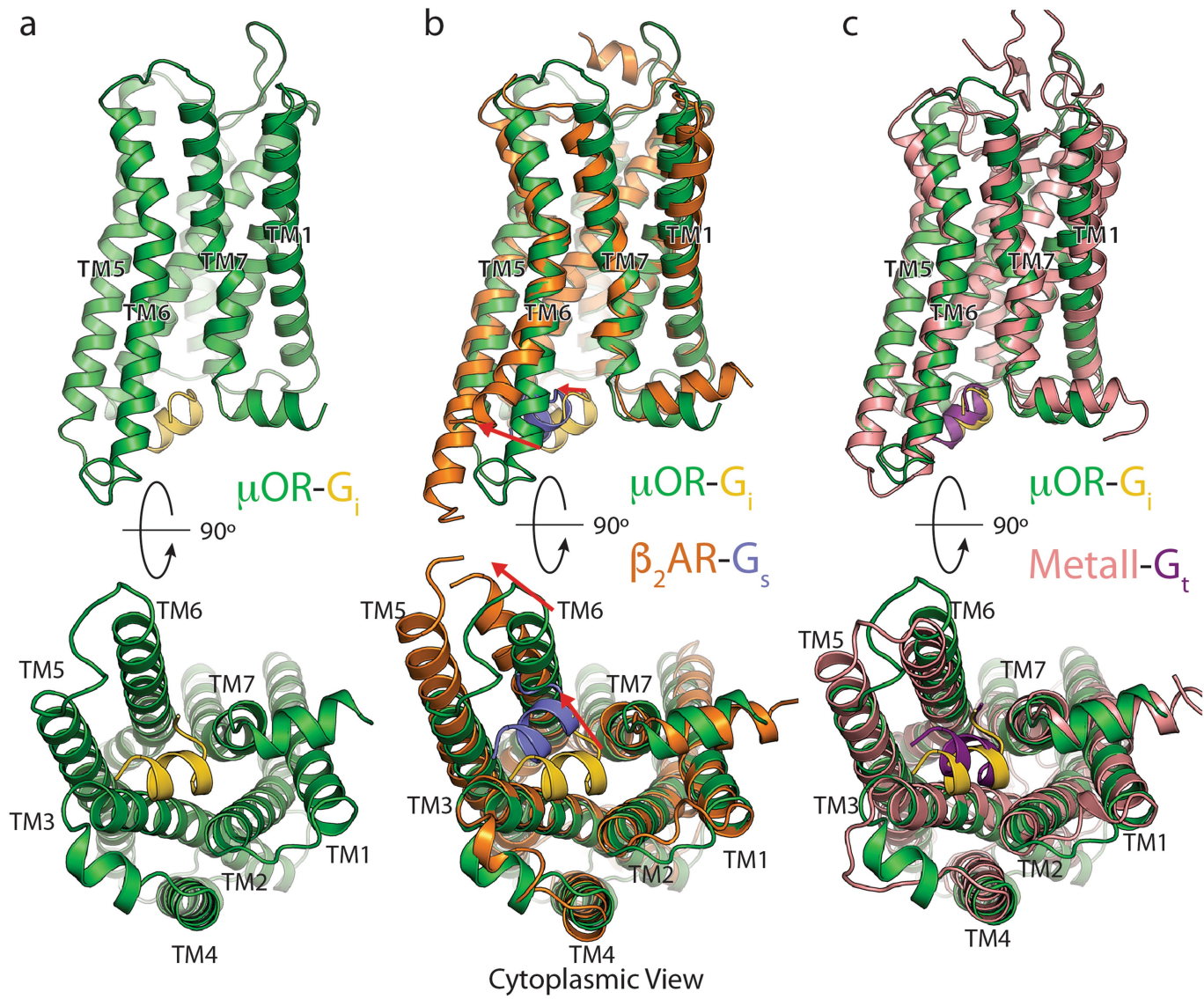
Extended Data Fig. 6 | Water occupancy in orthosteric binding site.
Left, water occupancy in molecular dynamics simulations of DAMGO-bound μ OR overlaid with a representative conformation from molecular dynamics simulations. Occupancy relative to bulk solvent is the ratio of the rate at which water is observed in a given volume to the rate at which water is expected to be observed in an equivalent volume in the bulk solvent.

For example, blue regions (occupancy ratio = 2) are occupied by water twice as often as an equivalent region in the bulk solvent. Right, crystallographic waters in the BU72-bound μ OR binding pocket (PDB code 5C1M). Waters are shown as black spheres, BU72 is shown as yellow sticks, and hydrogen bonds are shown as dashed lines.



Extended Data Fig. 7 | Comparison of the C termini of $G\alpha_s$ and $G\alpha_i$.
The C terminus of $G\alpha_s$ is bulkier than that of $G\alpha_i$ owing to substitution of small amino acids C (-4 position) and G (-3 position) in $G\alpha_i$ to Y and E, respectively, in $G\alpha_s$. This leads to steric clashes with TM3 and TM7 of the μ OR. Top, ribbon view of μ OR (green) with wild-type $G\alpha_i$ (gold, left) and

a $G\alpha_{is}$ model (right) created by substituting C and G for Y and E based on the β_2 AR- G_s crystal structure. Substituted positions are coloured in light purple. The -4 to -2 positions have their side chains shown as spheres, and the rest are shown as a ribbon. Bottom, space-filling view of the μ OR showing the steric clashes that result from these substitutions.



Extended Data Fig. 8 | Comparison of G α i C-terminal peptide binding modes. a–c, Side (top) and cytoplasmic (bottom) views of the μ OR (green) with the last 11 residues of G α i (gold) alone (a), compared to the β_2 AR (orange) with the last 11 residues of G α s (light purple) (PDB code 3SN6) (b), or compared to metarhodopsin II (pink) in complex with an

11-residue G α transducin (G α t) C-terminal peptide (dark purple) (PDB code 3PQR) (c). The μ OR–G α i complex aligns best with the metarhodopsin II–G α i complex in terms of both TM6 displacement and position of the α 5 peptide.

Extended Data Table 1 | Cryo-EM data collection, refinement and validation statistics

| | μ OR-G _i Complex (EMDB-7869) (PDB 6DDF) | μ OR-G _i -scFv16 Complex (EMDB-7868) (PDB 6DDE) |
|--|--|---|
| Data collection and processing | | |
| Magnification | 48,076 | 48,076 |
| Voltage (kV) | 300 | 300 |
| Electron exposure (e-/Å ²) | 40 | 40 |
| Defocus range (μm) | -0.8 ~ -2.6 | -0.8 ~ -2.6 |
| Pixel size (Å) | 1.04 | 1.04 |
| Symmetry imposed | C1 | C1 |
| Initial particle images (no.) | 893,426 | 893,426 |
| Final particle images (no.) | 359,406 | 359,406 |
| Map resolution (Å) | 3.5 Å | 3.6 Å |
| FSC threshold | (0.143) | (0.143) |
| Map resolution range (Å) | 3.3-4.5 | 3.3-4.5 |
| Refinement | | |
| Initial model used (PDB code) | 5C1M 1GP2 | 5C1M 1GP2 |
| Model resolution (Å) | 3.5 | 3.6 |
| Model resolution range (Å) | 3.3-4.5 | 3.3-4.5 |
| Map sharpening <i>B</i> factor (Å ²) | Pre -90, post -60 | Pre -90, post -60 |
| Model composition | | |
| Non-hydrogen atoms | 6986 | 8731 |
| Protein residues | 886 residues (6949 atoms) | 1119 residues (8694 atoms) |
| Ligands | 1 (37 atoms) | 1 (37 atoms) |
| <i>B</i> factors (Å ²) | | |
| Protein | 33.23 | 69.81 |
| Ligand | 31.27 | 100.66 |
| R.m.s. deviations | | |
| Bond lengths (Å) | 0.007 | 0.010 |
| Bond angles (°) | 1.303 | 1.328 |
| Validation | | |
| MolProbity score | 1.93 | 1.83 |
| Clashscore | 7.77 | 6.97 |
| Poor rotamers (%) | 0.72 | 0.46 |
| Ramachandran plot | | |
| Favored (%) | 91.54 | 93.02 |
| Allowed (%) | 8.35 | 6.89 |
| Disallowed (%) | 0.11% | 0.09% |

Extended Data Table 2 | Sequence alignment of residues that form the interaction interface between μ OR and G_i

| Mu-Opioid Receptor Residue | Coupling | Branch | | | | | | | | | | | | |
|----------------------------------|----------|----------|------|------|------|------|------|------|------|------|------|------|------|--|
| | | | T103 | V169 | P172 | V173 | D177 | R179 | T180 | M255 | K271 | R277 | I278 | |
| [Human] 5-HT1A receptor | Gi | α | A | I | P | I | N | R | T | I | A | K | T | |
| [Human] 5-HT1B receptor | Gi | α | A | I | A | V | A | R | T | I | M | K | A | |
| [Human] M2 receptor | Gi | α | N | V | P | L | V | R | T | I | P | K | V | |
| [Human] M4 receptor | Gi | α | N | V | P | L | A | R | T | I | M | K | V | |
| [Human] α 2A-adrenoceptor | Gi | α | Q | I | A | I | L | R | T | I | R | R | F | |
| [Human] FPR1 | Gi | γ | T | V | P | V | N | R | T | I | - | R | P | |
| [Human] FPR2/ALX | Gi | γ | T | V | P | V | N | R | T | I | - | R | P | |
| [Human] GAL1 receptor | Gi | γ | T | I | S | R | S | R | V | V | - | K | T | |
| [Human] GAL3 receptor | Gi | γ | T | V | P | L | A | R | T | T | R | R | A | |
| [Human] δ Opioid Receptor | Gi | γ | T | V | P | V | D | R | T | M | K | R | I | |
| [Human] κ Opioid Receptor | Gi | γ | T | V | P | V | D | R | T | M | K | R | I | |
| [Human] μ Opioid Receptor | Gi | γ | T | V | P | V | D | R | T | M | K | R | I | |
| [Human] NOP receptor | Gi | γ | T | I | P | I | D | R | T | M | K | R | I | |
| [Human] SST1 receptor | Gi | γ | T | V | P | I | R | R | R | I | R | K | I | |
| [Human] SST2 receptor | Gi | γ | T | V | P | I | K | R | R | I | R | K | V | |
| [Human] SST3 receptor | Gi | γ | T | V | P | T | R | R | T | I | R | R | V | |
| [Human] SST4 receptor | Gi | γ | T | V | P | L | T | R | R | I | R | K | I | |
| [Human] SST5 receptor | Gi | γ | T | V | P | L | R | R | R | I | - | K | V | |
| [Human] CCR1 | Gi | γ | T | I | A | V | R | R | T | I | - | K | A | |
| [Human] CCR4 | Gi | γ | T | I | A | V | R | R | T | I | - | K | A | |
| [Human] CXCR4 | Gi | γ | T | I | A | T | R | R | K | I | - | K | A | |
| [Human] A1 receptor | Gi | α | T | V | P | L | M | V | T | V | Y | K | I | |
| [Human] β 1-adrenoceptor | Gs | α | T | I | P | F | S | L | T | V | V | K | A | |
| [Human] β 2-adrenoceptor | Gs | α | T | I | P | F | S | L | T | V | F | K | A | |
| [Human] MC1 receptor | Gs | α | M | I | A | L | S | V | T | G | - | K | G | |
| [Human] MC2 receptor | Gs | α | M | I | A | L | S | V | T | K | - | K | G | |
| [Human] MC4 receptor | Gs | α | M | I | A | L | N | M | T | R | - | K | G | |
| [Human] A2A receptor | Gs | α | T | I | P | L | G | V | T | I | T | H | A | |
| [Human] H2 receptor | Gs | α | T | V | P | L | V | V | T | I | A | K | A | |
| [Human] TA1 receptor | Gs | α | T | V | P | L | A | M | N | I | S | K | A | |
| [Human] RXFP1 | Gs | δ | Y | I | P | F | R | - | G | M | Q | I | L | |
| [Human] RXFP2 | Gs | δ | H | I | P | F | R | - | G | M | C | A | V | |
| [Human] V2 receptor | Gs | β | I | I | P | M | R | G | S | I | V | K | T | |
| [Human] 5-HT2A receptor | Gq | α | T | I | P | I | R | N | S | T | S | K | A | |
| [Human] 5-HT2B receptor | Gq | α | T | I | P | I | Q | N | S | T | T | R | A | |
| [Human] M1 receptor | Gq | α | N | V | P | L | A | R | T | I | S | K | A | |
| [Human] M3 receptor | Gq | α | N | I | P | L | A | R | T | I | S | K | A | |
| [Human] M5 receptor | Gq | α | N | I | P | L | A | R | T | I | V | K | A | |
| [Human] α 1A-adrenoceptor | Gq | α | T | V | P | L | T | V | T | V | K | K | A | |
| [Human] GAL2 receptor | Gq | γ | T | I | P | L | E | R | T | T | A | K | V | |
| [Human] OX1 receptor | Gq | β | T | I | P | L | - | - | T | I | Q | K | T | |
| [Human] OX2 receptor | Gq | β | T | I | P | L | - | - | T | I | Q | K | T | |
| [Human] NK1 receptor | Gq | β | T | I | - | - | - | - | S | V | Q | K | V | |

Receptors from different branches of the GPCR family with different coupling specificities were selected for analysis. Sequences and alignment were performed using GPCRDB (<http://www.gpcrdb.org>)

Reporting Summary

Nature Research wishes to improve the reproducibility of the work that we publish. This form provides structure for consistency and transparency in reporting. For further information on Nature Research policies, see [Authors & Referees](#) and the [Editorial Policy Checklist](#).

Statistical parameters

When statistical analyses are reported, confirm that the following items are present in the relevant location (e.g. figure legend, table legend, main text, or Methods section).

n/a Confirmed

- The exact sample size (n) for each experimental group/condition, given as a discrete number and unit of measurement
- An indication of whether measurements were taken from distinct samples or whether the same sample was measured repeatedly
- The statistical test(s) used AND whether they are one- or two-sided
Only common tests should be described solely by name; describe more complex techniques in the Methods section.
- A description of all covariates tested
- A description of any assumptions or corrections, such as tests of normality and adjustment for multiple comparisons
- A full description of the statistics including central tendency (e.g. means) or other basic estimates (e.g. regression coefficient) AND variation (e.g. standard deviation) or associated estimates of uncertainty (e.g. confidence intervals)
- For null hypothesis testing, the test statistic (e.g. F , t , r) with confidence intervals, effect sizes, degrees of freedom and P value noted
Give P values as exact values whenever suitable.
- For Bayesian analysis, information on the choice of priors and Markov chain Monte Carlo settings
- For hierarchical and complex designs, identification of the appropriate level for tests and full reporting of outcomes
- Estimates of effect sizes (e.g. Cohen's d , Pearson's r), indicating how they were calculated
- Clearly defined error bars
State explicitly what error bars represent (e.g. SD, SE, CI)

Our web collection on [statistics for biologists](#) may be useful.

Software and code

Policy information about [availability of computer code](#)

Data collection

Automated data collection on the Titan Krios was performed using serialEM

Data analysis

The following software was used in this study: MotionCor2, gCTF v1.06, RELION 2.1, FREALIGN, cisTEM, BSoft, UCSF Chimera, UCSF ChimeraX, Coot, Pymol, Phenix, Rosetta, PRODRG Server, AMBER17, VIPER

For manuscripts utilizing custom algorithms or software that are central to the research but not yet described in published literature, software must be made available to editors/reviewers upon request. We strongly encourage code deposition in a community repository (e.g. GitHub). See the Nature Research [guidelines for submitting code & software](#) for further information.

Data

Policy information about [availability of data](#)

All manuscripts must include a [data availability statement](#). This statement should provide the following information, where applicable:

- Accession codes, unique identifiers, or web links for publicly available datasets
- A list of figures that have associated raw data
- A description of any restrictions on data availability

All data generated or analyzed during this study are included in this published article and its Supplementary Information. Sequences of constructs used in this study

are listed in Supplementary Figure 1. The cryo-EM density maps for the mOR-Gi complex with, and without scFv16 have been deposited in the Electron Microscopy Data Bank under accession codes EMD-XXXX and EMD-YYYY respectively. The coordinates for the models of mOR-Gi with, and without scFv16 have been deposited in the Protein Data Bank under accession codes XXXX and YYYY, respectively.

Field-specific reporting

Please select the best fit for your research. If you are not sure, read the appropriate sections before making your selection.

Life sciences Behavioural & social sciences

For a reference copy of the document with all sections, see nature.com/authors/policies/ReportingSummary-flat.pdf

Life sciences

Study design

All studies must disclose on these points even when the disclosure is negative.

| | |
|-----------------|---|
| Sample size | Sample size was not pre-determined by any statistical metrics. Sample size was limited by time allocation on microscopes, subsequent processing of images confirmed we had enough data to reach high resolution. |
| Data exclusions | No data was systematically excluded. Over the course of refinement of our maps, particles with low signal, or particles that did not align well to the consensus map were excluded from final map calculations as implemented in RELION 2.1 and FREALIGN. |
| Replication | No replication studies were attempted, nor were necessary. Our primary data is a cryo-EM structure that was calculated according to standard procedures and does not need replicates. |
| Randomization | No randomization was necessary for this study. Our primary data is a calculated cryo-EM structure that was calculated according to standard procedures with freely available software and does not need randomization. |
| Blinding | No blinding was used or necessary during data collection or analysis. As above, Our primary data is a calculated cryo-EM structure that was calculated according to standard procedures with freely available software and did not require blinding. We calculated our initial model ab-initio to avoid bringing model bias into our map calculation, and in a sense, blinded the software. |

Materials & experimental systems

Policy information about [availability of materials](#)

| | |
|-------------------------------------|---|
| n/a | Involved in the study |
| <input type="checkbox"/> | <input checked="" type="checkbox"/> Unique materials |
| <input type="checkbox"/> | <input checked="" type="checkbox"/> Antibodies |
| <input type="checkbox"/> | <input checked="" type="checkbox"/> Eukaryotic cell lines |
| <input type="checkbox"/> | <input checked="" type="checkbox"/> Research animals |
| <input checked="" type="checkbox"/> | <input type="checkbox"/> Human research participants |

Unique materials

Obtaining unique materials scFv16 is the property of F. Hoffmann-La Roche Ltd (Roche) and is available upon request by MTA.

Antibodies

| | |
|-----------------|---|
| Antibodies used | scFv16 came from an antibody (mAb-16) that binds the Gi heterotrimer. This antibody was generated by Roger Dawson at F Hoffmann-La Roche Ltd (Roche). As above, it is available upon request by MTA. |
| Validation | Binding was confirmed by size-exclusion chromatography on purified protein, as well as by ELISA. Sequencing was performed on mouse hybridoma cells producing mAb16 and the scFv fragment was cloned. Binding of this scFv fragment was confirmed by size exclusion chromatography and electron microscopy. This antibody was generated for the purposes of this study. Most of the scFv could be built into density and register was confirmed. |

Eukaryotic cell lines

Policy information about [cell lines](#)

| | |
|---------------------|---|
| Cell line source(s) | Sf9, Expression Systems, Cat 94-001S. Tni Cells (Hi-5), Expression Systems, Cat 94011S. PAI mouse myeloma cell lines (a variant of the P3-x63-AG8 myeloma) as : PAI (RRID:CVCL_J288). The myeloma cells were obtained from the Basel Institute of Immunology. |
|---------------------|---|

Authentication

Cell lines are maintained by the supplier. No additional authentication was performed by the authors of this study.

Mycoplasma contamination

Cell lines are tested by manufacturer for contamination, but not were not further tested by the authors of this study. The mouse myeloma cells are tested by manufacturer for ectromelia virus (mousepox).

**Commonly misidentified lines
(See [ICLAC](#) register)**

None used.

Research animals

Policy information about [studies involving animals](#); [ARRIVE guidelines](#) recommended for reporting animal research

Animals/animal-derived materials

Initially, 4 female BALB/c mice (*mus musculus*) at 6-8 weeks of age were immunized with the Rhodopsin-Gi complex, and two showed good responses. These two were sacrificed for splenocyte isolation.

Method-specific reporting

n/a Involved in the study

- | | |
|-------------------------------------|---|
| <input checked="" type="checkbox"/> | <input type="checkbox"/> ChIP-seq |
| <input checked="" type="checkbox"/> | <input type="checkbox"/> Flow cytometry |
| <input checked="" type="checkbox"/> | <input type="checkbox"/> Magnetic resonance imaging |